

# TEMPERATURE AND PRESSURE DEPENDENCES OF THE PROPERTIES AND PHASE TRANSITION IN PARATELLURITE ( $\text{TeO}_2$ ): ULTRASONIC, DIELECTRIC AND RAMAN AND BRILLOUIN SCATTERING RESULTS†

P. S. PEERCY, I. J. FRITZ and G. A. SAMARA  
Sandia Laboratories, Albuquerque, NM 87115, U.S.A.

(Received 6 December 1974)

**Abstract**—The effects of temperature and pressure on the ultrasonic propagation properties, dielectric constants and the Raman and Brillouin spectra in paratellurite ( $\text{TeO}_2$ ) were investigated with emphasis on the behavior in the vicinity of the newly-discovered, pressure-induced phase transition. The transition is found to be second-order and purely strain-induced, driven by a soft shear acoustic mode propagating along a  $\langle 110 \rangle$  and polarized along a  $\langle \bar{1}\bar{1}0 \rangle$  crystal direction. Such pure-strain transitions were previously discussed by Anderson and Blount and the transition in paratellurite is the first observation of this kind of transition. No evidence was found for any coupling of the soft mode to any other acoustic or optic mode, although small anomalies associated with lattice strains accompanying the transition were observed in some of the elastic and dielectric constants. Analysis of the effective elastic constant  $C'$  governing the soft mode velocity indicates that, within experimental uncertainty, the transition can be described by mean-field theory. Although the apparent attenuation of the soft mode increased significantly near the transition, it is concluded that this effect is probably due to the fact that the phase and group velocities are not parallel rather than to intrinsic dissipative processes in the crystal. With the exception of  $C_{44}$ , the remaining elastic constants and Raman-active phonon frequencies displayed normal increases with pressure. No soft Raman-active modes were observed in either phase. The static dielectric constants  $\epsilon_i$  are large, due to the large electronic polarizability of  $\text{TeO}_2$ , and the anisotropy in  $\epsilon$  results almost entirely from the anisotropy in the optical dielectric constants  $\epsilon_\infty$ . In the low pressure tetragonal phase both  $\epsilon_a$  and  $\epsilon_c$  exhibit normal temperature dependences and  $\epsilon_c$  decreases with pressure; however,  $\epsilon_a$  exhibits an anomalous increase with pressure. Temperature, pressure and uniaxial stress measurements are combined to evaluate the various contributions to the temperature and pressure dependences of  $\epsilon$ . Combining the  $\epsilon$  data with available i.r. measurements demonstrated that the generalized Lyddane-Sachs-Teller relation is well obeyed for  $\text{TeO}_2$ . Finally, the Szigetti effective charge ratios were determined for the lowest frequency IR-active modes. These ratios were found to be quite low, being 0.27 and 0.18 for the  $a$ -axis responses, respectively, indicating that the bonding is highly covalent.

## 1. INTRODUCTION

Tellurium dioxide ( $\text{TeO}_2$ ) crystallizes in three different structures at atmospheric pressure—an orthorhombic structure of  $D_{2h}^{15}$  symmetry and two tetragonal structures of symmetry  $D_{4h}^{15}$  (rutile structure) and  $D_4^4$  (paratellurite). Large single crystals of excellent optical quality have been grown of the paratellurite structure, and this material has received considerable attention for piezoelectric and electrooptic applications.

Peercy and Fritz[1] recently demonstrated that paratellurite undergoes an apparently ideal second-order pressure induced phase transition at  $\sim 9$  kbar at room temperature. They suggested that the transition is driven by a soft acoustic shear mode and noted that, if this were the case, the high pressure structure would be of orthorhombic  $D_2$  symmetry. Worlton and Beyerlein[2] have subsequently measured the pressure dependence of elastic neutron scattering from paratellurite and find that the structure of the high pressure phase is indeed orthorhombic ( $D_2^2$  symmetry) with neither a discontinuous volume change nor a change in the number of atoms

in the unit cell at the phase transition. Their results are consistent with the phase transition being second-order.

This transition is unique since it is a reversible second order transition which can be induced with pressure but not with temperature at atmospheric pressure; furthermore, the transition appears to be purely strain-induced, driven by a soft shear acoustic mode propagating along a  $\langle 110 \rangle$  crystal direction and polarized along a  $\langle \bar{1}\bar{1}0 \rangle$  crystal direction. Such pure strain transitions were discussed by Anderson and Blount[3] and paratellurite apparently represents the first observation of this type of transition. A similar strain induced transition has very recently been observed in  $\text{PrAlO}_3$  as a function of temperature by Fleury, Lazay and Van Uitert[4].

The velocity of the soft shear mode in paratellurite is determined by the combination of elastic constants  $C' = \frac{1}{2}(C_{11} - C_{12})$ . The mode has a low velocity ( $V_s = 0.61 \times 10^5$  cm/sec) at atmospheric temperature and pressure by virtue of the near cancellation of  $C_{11}$  and  $C_{12}$  and softens slightly with decreasing temperature. The pressure dependence of the soft mode was measured using ultrasonic velocity and Brillouin scattering techniques, and the pressure dependences of the static dielectric constants and Raman-active phonons were investigated for possible interaction between the optic modes and the

†This work was supported by the United States Atomic Energy Commission.

soft acoustic mode. Preliminary results of these measurements were previously reported[1].

We have extended these measurements to give a more complete description of the phase transition as well as to examine the various lattice and dielectric properties of this material. The soft mode velocity and attenuation were investigated near the transition and the pressure dependences of the different elastic constants, with the exception of  $C_{13}$ , were measured throughout the low pressure (tetragonal) phase using ultrasonic velocity and Brillouin scattering techniques. The ultrasonic velocity measurements were extended to the high pressure (orthorhombic) phase for those modes which gave reliable echoes in this phase. The pressure dependences of the Raman-active optic phonons were measured up to 10 kbar which allowed us to evaluate the mode Grüneisen parameters as well as to investigate these spectra for any anomalies associated with the transition. Finally, detailed measurements were made of the pressure and temperature dependences of both the *a*- and *c*-axis dielectric constants. These measurements were used to explore the pressure-temperature phase boundary and were combined with uniaxial stress measurements of the dielectric constants to examine the anharmonic contributions to the infrared-active phonon modes. The purpose of this paper is to present and discuss the results of these measurements.

The paper is arranged as follows: Section 2 contains a discussion of the symmetry of the optic and acoustic modes in the low pressure phase. The experimental arrangements are given in Section 3 and the experimental results are presented and discussed in Section 4; details of the phase transition are summarized in Section 5.

2. SYMMETRY OF THE NORMAL MODES

(a) Optic modes

Paratellurite crystallizes in a distorted rutile structure of  $D_4^h(P4_2,2)$  symmetry at atmospheric pressure[5]. The unit cell, which contains four  $\text{TeO}_2$  molecules, is shown schematically in Fig. 1. Paratellurite therefore has 36 long

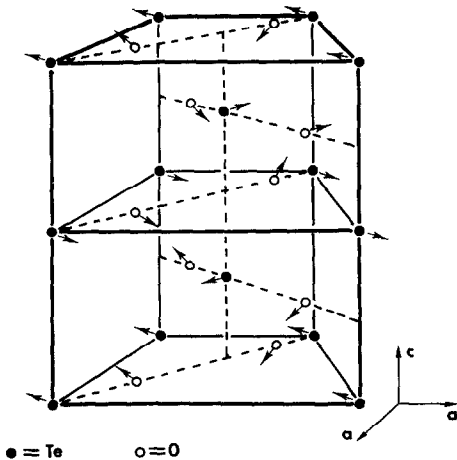


Fig. 1. Schematic representation of the crystal structure of  $\text{TeO}_2$ , visualized as a distortion of the doubled rutile unit cell. The arrows indicate the distortions required to obtain the  $\text{TeO}_2$  structure from the rutile structure.

wavelength ( $q=0$ ) lattice modes with the irreducible representation in the tetragonal ( $D_4$ ) phase[6-8]

$$\Gamma = 4A_1 + 5A_2 + 5B_1 + 4B_2 + 9E. \tag{1}$$

The modes of *E* symmetry are doubly degenerate. For the wavevector *q* parallel to a crystal axis, the three acoustic modes have symmetry

$$\Gamma_{ac} = A_2 + E \tag{2}$$

which leaves 33 optic modes with the irreducible representation

$$\Gamma_0 = 4A_1 + 4A_2 + 5B_1 + 4B_2 + 8E. \tag{3}$$

Modes of symmetry  $A_1$ ,  $B_1$ ,  $B_2$  and *E* are Raman-active with polarizability tensors

$$\begin{aligned} \alpha(A_1) &= \begin{pmatrix} a & \cdot & \cdot \\ \cdot & a & \cdot \\ \cdot & \cdot & b \end{pmatrix}, \\ \alpha(B_1) &= \begin{pmatrix} c & \cdot & \cdot \\ \cdot & -c & \cdot \\ \cdot & \cdot & \cdot \end{pmatrix}, \quad \alpha(B_2) = \begin{pmatrix} \cdot & d & \cdot \\ d & \cdot & \cdot \\ \cdot & \cdot & \cdot \end{pmatrix}, \\ \alpha(E_x) &= \begin{pmatrix} \cdot & \cdot & \cdot \\ \cdot & \cdot & e \\ \cdot & e & \cdot \end{pmatrix}, \quad \alpha(E_y) = \begin{pmatrix} \cdot & \cdot & -e \\ \cdot & \cdot & \cdot \\ -e & \cdot & \cdot \end{pmatrix} \end{aligned} \tag{4}$$

while modes of symmetry  $A_2$  and *E* are i.r.-active. All of the optic modes are therefore either Raman or i.r.-active and can be completely determined by a combination of i.r. and Raman scattering measurements.

(b) Acoustic modes

The elastic and long wavelength acoustic properties of the low pressure  $D_4$  phase of paratellurite are determined by six independent elastic constants:  $C_{11}$ ,  $C_{12}$ ,  $C_{13}$ ,  $C_{33}$ ,  $C_{44}$  and  $C_{66}$ . Values for these constants and their temperature dependences have been previously reported[9, 10]. We have measured and pressure dependences of all the elastic constants except  $C_{13}$ ; Table 1 lists the various acoustic modes used to study the elastic constants in our ultrasonic velocity and Brillouin scattering measurements.

Table 1. Acoustic wave propagation properties for selected modes in the tetragonal phase of paratellurite

Propagation Direction ( <i>q</i> )	Mode Type and Polarization	Designation	Effective elastic constant $c^* = \rho v^2$
$\langle 100 \rangle$	L $\langle 100 \rangle$	Mode 1	$C_{11}$
$\langle 100 \rangle$	S $\langle 010 \rangle$	Mode 2	$C_{66}$
$\langle 100 \rangle$	S $\langle 001 \rangle$	Mode 3	$C_{44}$
$\langle 110 \rangle$	S $\langle \bar{1}10 \rangle$	Mode 4	$\frac{1}{2}(C_{11}-C_{12}) = C'$
$\langle 110 \rangle$	S $\langle 001 \rangle$	Mode 5	$C_{44}$
$\langle 001 \rangle$	L $\langle 001 \rangle$	Mode 6	$C_{33}$
$\langle 001 \rangle$	S $\langle \text{any} \rangle$	Mode 7	$C_{44}$

The mode velocities  $V$  are governed by the relation  $\rho V^2 = C^*$  where  $\rho$  is the mass density and  $C^*$  is the effective elastic constant for the mode. Mode 4 is the soft mode for the structural phase transition at 8.9 kbar.

Since paratellurite is piezoelectric [9], the possibility of piezoelectric coupling effects must be considered in discussing acoustic wave propagation. Two types of piezoelectric effects may be important:

(1) Piezoelectric coupling may cause certain modes to be mixed acoustic-electromagnetic waves. In this case an electric field component parallel to  $q$  causes elastic "stiffening" of the wave [11, 12]. This stiffening can be taken into account by replacing the usual zero field elastic constant tensor  $C_{ijkl}$  by an effective elastic constant tensor  $C_{ijkl}^E = C_{ijkl}^0 + A_{ijkl}$  where  $A_{ijkl}$  is given in terms of the piezoelectric tensor  $e_{ijk}$ , the constant strain permittivity tensor  $\epsilon_{ij}^s$ , and the direction cosines  $n_i$  of the propagation wave vector by the expression

$$A_{ijkl} = \frac{e_{pij}e_{qkl}}{\epsilon_{rs}^s n_r n_s} n_p n_q. \quad (5)$$

The only nonzero piezoelectric coefficients of paratellurite are (in Voigt notation)  $e_{14} = -e_{25}$ . The contribution of  $A$  to the Cristoffel tensor is

$$(A_{ijkl}n_jn_k) = \frac{e_{14}^2 n_3^2}{\epsilon_{rs}^s n_r n_s} \begin{pmatrix} n_2^2 n_3^2 & -n_1 n_2 n_3^2 & 0 \\ -n_1 n_2 n_3^2 & n_1^2 n_3^2 & 0 \\ 0 & 0 & 0 \end{pmatrix}. \quad (6)$$

Thus there is no stiffening for propagation perpendicular to the  $c$ -axis ( $n_3 = 0$ ) or parallel to the  $c$ -axis ( $n_1 = n_2 = 0$ ) in paratellurite. Since all of the modes we investigated propagate either parallel or perpendicular to the  $c$ -axis (Table 1), there is no piezoelectric stiffening for any of these modes so that all modes measured yield zero field ( $C_{ij}^E$ ) elastic constants.

(2) Piezoelectric coupling may produce coupled strain-polarization modes. This effect is important in certain piezoelectric materials which have dielectric anomalies associated with ferroelectric transitions (e.g. KH<sub>2</sub>PO<sub>4</sub>) [13, 14]. In this case, the mode in question need not be piezoelectrically stiffened as above. A constant field elastic constant therefore determines the wave velocity but the constant field coefficient itself can have anomalous behavior because of anomalous dielectric behavior. In paratellurite, any mode involving an  $x_4$  strain component is piezoelectrically coupled to the  $a$ -axis dielectric constant  $\epsilon_a$ . (For example, the  $C_{44}$  shear modes 3, 5 and 7 of Table 1 are pure  $x_4$  shear modes; furthermore, these are the only modes in Table 1 which exhibit any piezoelectric coupling effects.) Then,

$$C_{44}^E = C_{44}^P - \frac{a_{14}^2 \epsilon_a}{4\pi} \quad (7)$$

where  $C_{44}^P$  is the elastic constant at constant electric polarization and the piezoelectric coefficient  $a_{14} = (4\pi/\epsilon_a)e_{14}$ . Thus if  $a_{14}$  and  $C_{44}^P$  exhibit "normal" temperature and pressure dependences (as do the analogous quantities in KH<sub>2</sub>PO<sub>4</sub>) then any anomalous behavior

observed for  $C_{44}^E$  and  $\epsilon_a$  may be related. As we shall see below, both  $C_{44}^E$  and  $\epsilon_a$  exhibit anomalous pressure dependences, but it is not clear whether eqn (7) explains these results with  $C_{44}^P$  and  $a_{14}$  having normal behavior, since neither  $C_{44}^P$  nor  $a_{14}$  have been measured.

Neutron diffraction [2] and X-ray measurements [15] indicate that the high pressure phase of paratellurite has orthorhombic  $D_2(P222)$  symmetry. For this symmetry there are three additional independent elastic constants  $C_{22}$ ,  $C_{23}$  and  $C_{55}$  which "evolve" from  $C_{11}$ ,  $C_{13}$  and  $C_{44}$ , respectively, and an additional piezoelectric constant  $e_{36}$  "evolves" from zero at the transition. However, because of domain formation in the high pressure phase, it was not generally possible to determine the elastic constants from ultrasonic or Brillouin measurements.

### 3. EXPERIMENTAL CONSIDERATIONS

#### (a) Samples

All measurements were made on oriented single crystal samples obtained from Crystal Technology, Inc. [16] Raman and Brillouin spectra were obtained using single crystal cubes with dimensions of  $5 \times 5 \times 5$  mm. The Brillouin spectra were measured for phonon propagation  $\hat{q}$  along the principal crystallographic directions as indicated in Table 1, and this was sufficient to examine the pressure dependence of each elastic constant except  $C_{13}$ . Because all measurements were taken with a scattering angle of  $90^\circ$ , three different crystal orientations were required, with crystal faces normal to: (1)  $\langle 100 \rangle$ ,  $\langle 010 \rangle$  and  $\langle 001 \rangle$ , (2)  $\langle 110 \rangle$ ,  $\langle 1\bar{1}0 \rangle$  and  $\langle 001 \rangle$ , and (3)  $\langle 010 \rangle$ ,  $\langle 101 \rangle$  and  $\langle 10\bar{1} \rangle$  axes. Raman spectra were recorded using the same crystal orientations because of the  $L0-T0$  splittings of the  $E$  modes [7].

Several samples of different dimensions were used for the ultrasonic measurements. Sample thicknesses between 1.3 and 5 mm were used to study the soft mode, and ultrasonic path lengths of  $\sim 5$  mm were used to study the other modes.

The samples used for the dielectric measurements were typically  $0.3$  to  $0.8$  cm<sup>2</sup> in area and  $0.06$  to  $0.09$  cm thick with either the  $a$ - or  $c$ -axis perpendicular to the large faces. These faces were vapor coated with gold electrodes.

#### (b) Raman and Brillouin scattering

The Raman spectra were obtained with a conventional Raman scattering arrangement. Light from an argon laser operating at  $4880 \text{ \AA}$  with incident power  $\sim 200$  mW was focused into the polished single crystal. Light scattered at  $90^\circ$  to the incident beam was analyzed with a double grating spectrometer and detected with a cooled photomultiplier. Signals from the photomultiplier were measured using photon counting electronics and stored in a multichannel analyzer.

The Brillouin spectra were also obtained in a  $90^\circ$  scattering geometry. The spectra were excited with the argon laser operating in a single mode at  $4880 \text{ \AA}$  and the scattered light was analyzed with a piezoelectrically scanned Fabry Perot with flat mirrors. The Fabry Perot had an operating finesse of  $\sim 50$  and various free spectral ranges between  $0.3$  and  $1.5 \text{ cm}^{-1}$  were used. As in the

Raman scattering measurements, signals from the photo-multiplier were measured using photon counting electronics and stored in a multichannel analyzer.

The hydrostatic pressure optical cell used in these experiments was of a design provided by W. B. Daniels. The cell was made of nickel maraging steel and had three optic windows of single crystal sapphire to allow a 90° scattering geometry. The samples were immersed in the pressure fluid (Isopar H, Humble Oil Co.), and the pressure was measured to  $\pm 50$  psi with a Heise Bourdon tube gauge for pressures up to 75,000 psi. At higher pressures, the pressure was measured to  $\pm 1\%$  with a manganin coil.

### (c) Ultrasonic measurements

The following ultrasonic measurements were made as a function of pressure at room temperature: (1) the soft mode (mode 4) velocity  $V^2 = (1/2\rho)(C_{11} - C_{12})$  from 0 to 12 kbar, (2) the soft mode attenuation from 0 to 8.9 kbar, and (3) velocities of modes 1, 2, 3 and 6 to 8.9 kbar (and higher pressures wherever possible). The pressure dependences of the elastic constants were measured relative to the atmospheric pressure values.

Ultrasonic velocity and attenuation were measured using standard pulse echo techniques. For the velocity measurements, the unrectified echo trains were displayed on an oscilloscope and delay times between successive echoes, or between the first echo and a reference fiducial mark, were measured using the calibrated delay potentiometer of the oscilloscope. Near the phase transition the acoustic pulses for the soft mode were very distorted, with the leading edge being strongly attenuated. The *rf* cycles at the beginning of the pulse were lost in the noise, and to obtain accurate velocity data it was necessary to measure later cycles in the pulse and to apply appropriate transit time corrections. Measurements made by locating the peak (or leading edge) of a rectified pulse would have yielded transit times which were too large near the transition.

Attenuation data were obtained for the soft mode by comparing the amplitude of a given echo pulse with a signal from an amplitude calibrated Hewlett Packard Model 606B signal generator[17].

The transducers were coaxially plated X- or AC-cut quartz discs of  $\sim 6$  mm diameter and  $\sim 3$  mm diameter active area. The soft mode velocity was measured at 2 and 5 MHz and the soft mode attenuation was measured at 10 and 70 MHz. Other mode velocities were measured at 30 MHz. Phthalic-anhydride glycerin polymer was used for a bonding agent.

Pressure was produced with a 30 kbar Bridgman press using a 50–50 mixture of *n*-pentane and isopentane[18]. The pressure was measured to an accuracy of  $\pm 1\%$  with a manganin gauge which was calibrated against the Bi I  $\rightarrow$  II transition.

### (d) Dielectric measurements

The dielectric constants were determined from capacitance measurements performed at 1–100 kHz using a General Radio Model 1615-A transformer ratio arm capacitance bridge with three terminal connections and

having an accuracy better than 0.1%. Shielded leads and sample holders were used.

Pressure experiments at and above room temperature were performed in the 30-kbar apparatus. The general experimental procedures have been given elsewhere[18].

Measurements below room temperature were performed in beryllium copper or maraging steel cells mounted inside conventional low temperature dewars. These cells are capable of pressure up to 5 and 10 kbar, respectively. Helium gas was the pressure fluid and the pressure was measured to better than 1% by a Heise Bourdon tube gauge and a calibrated manganin gauge. Temperature changes were measured (to  $\pm 0.1^\circ\text{K}$ ) using Cu-constantan thermocouples down to  $\sim 40^\circ\text{K}$  and Cu–AuFe thermocouples (to  $\pm 0.1^\circ\text{K}$ ) at lower temperatures.

The measurements consisted of the temperature dependences of  $\epsilon_a$  and  $\epsilon_c$  at 1 bar from 4–300°K and at 9.3 kbar from 76–300°K and the pressure dependences of  $\epsilon_a$  and  $\epsilon_c$  (up to 23 kbar in few cases) at 76, 295 and 353°K.

Uniaxial stress measurements were also performed at 295°K. Compressive force was applied along either the *a*- or *c*-axis by means of a micrometer adjustment, with the sample held between two optically flat nickel maraging steel plates, and measured by a W. C. Dillon model U force gauge[19]. The micrometer and gauge were contacted to the plates with ball bearings to help achieve uniaxial stress.

## 4. RESULTS AND DISCUSSION

### (a) Compressibility and thermal expansion

To analyze the pressure and temperature data it is necessary to take into account the changes in the sample volume with pressure and temperature. These dimensional corrections are easily made if the axial compressibilities  $\kappa_i$  and thermal expansivities  $\beta_i$  are known. Since our elastic constants are measured relative to the 1 bar values of Ohmachi and Uchida[9], these elastic constants and the low pressure compressibilities calculated from them are given in Table 2. Table 2 also includes other previously measured parameters (thermal expansivities, elastic compliances and photoelastic constants) which are used later in our analysis.

The  $\beta_i$  were measured down to  $\sim 120^\circ\text{K}$  and it was necessary to extrapolate the data to lower temperature to analyze our  $\epsilon(T)$  measurements. Any small uncertainties resulting from this extrapolation are negligible for the present purposes. Representative values for  $\beta_a(\beta_c)$  in units of  $10^{-6}/^\circ\text{K}$  are: 20.0(6.6), 18.6(5.8), 17.1(4.5) and 16.3(3.5) at 295, 223, 123 and 73°K, respectively. Similarly, it was necessary to extrapolate  $\kappa_a$  and  $\kappa_c$  to lower temperatures and the 75.6°K values used in the present analysis are  $\kappa_a = 6.11 \times 10^{-4}/\text{kbar}$  and  $\kappa_c = 6.15 \times 10^{-4}/\text{kbar}$ . We also note that the elastic constants yield adiabatic compressibilities, but the small differences between these and the needed isothermal compressibilities are negligible for our purposes.

The  $\kappa_i$  are expected to exhibit some pressure dependence; however we could not evaluate this from our elastic constant measurements since we did not measure  $C_{13}(P)$ . In our analysis, we therefore used Worlton and

Table 2. Compressibilities, thermal expansivities and the elastic and photoelastic properties at 0.63 μ of TeO<sub>2</sub> at 295°K

$\eta_{ij}$	$a$	$a$	$b$	$\pi_{ij}$	Compressibilities		
	$C_{ij}$	$S_{ij}$	$P_{ij}$		$\kappa_a$	$\kappa_c$	$\kappa_v$
	(10 <sup>2</sup> /kbar)	(10 <sup>-3</sup> /kbar)	(at 0.63μ)	(10 <sup>-4</sup> /kbar)	(10 <sup>-4</sup> /kbar)	(10 <sup>-4</sup> /kbar)	(10 <sup>-4</sup> /kbar)
$\eta_{11}$	5.57	11.50	0.0074	-1.95	8.11	6.11	22.33
$\eta_{12}$	5.12	-10.48	0.187	2.00	Expansivities		
$\eta_{13}$	2.18	-0.211	0.340	0.309			
$\eta_{33}$	10.58	1.03	0.240	0.209			
$\eta_{44}$	2.65	3.77	0.170				
$\eta_{66}$	6.59	1.52	-0.0463				
$\eta_{31} = C_{13}$		$S_{13}$	0.0905	0.0443	$\beta_a$	$\beta_c$	$\beta_v$
					(10 <sup>-6</sup> /°K)	(10 <sup>-6</sup> /°K)	(10 <sup>-6</sup> /°K)
					20.0	6.6	46.6

a. Ref. 9

b. Ref. 24

Beyerlein's measurements of the pressure dependences of the lattice parameters. The fractional changes in the lattice parameters with pressure determined from their neutron diffraction data are given in Table 3. There is substantial scatter in the c-axis data so we assumed a constant value for  $\kappa_c$  (6.11 × 10<sup>-4</sup>/kbar) throughout the tetragonal phase.

(b) Ultrasonic measurements

1. Data analysis. Analysis of the high pressure ultrasonic velocity data consists of deducing elastic constants as a function of pressure from the measured transit times for propagation of ultrasonic pulses through the sample. The pressure dependence of an effective elastic constant C\* is governed by the expression

C\* = C<sub>0</sub><sup>\*</sup> ρ / ρ<sub>0</sub> (l/l<sub>0</sub>)<sup>2</sup> (8)

where ρ is the mass density, l is the acoustic path length and t is the transit time. The zero subscripts in eqn (8) refer to the 1 bar values of the various quantities while the unsubscripted quantities represent the values at finite

Table 3. Compression data for TeO<sub>2</sub> based on Worlton and Beyerlein's smoothed data. a<sub>0</sub> = 4.8105 Å and c<sub>0</sub> = 7.6140 Å

P (kbar)	(a/a <sub>0</sub> )	(c/c <sub>0</sub> )
0	1.000	1.0000
4	.9972	.99764
6	.99574	.99672
7	.99491	.99593
8	.99428	.99514
8.85	.99366	.99475
9.5	.99262*	.99396
10	.99179*	.99343
12	.87971*	.99212
15	.98659*	.99094
19	.98368*	.99015
23	.98223*	.99015

\*In the orthorhombic phase, we take a = ½(a+b).

pressure. We did not measure the absolute value of C<sub>0</sub><sup>\*</sup> but evaluated it from the data of Ohmachi and Uchida[9] (Table 2) which is in good agreement with the data of Arlt and Schweppe[10]. The variations in ρ/ρ<sub>0</sub> and l/l<sub>0</sub> with pressure were calculated assuming  $\kappa_a$  and  $\kappa_c$  were constant with pressure, yielding linear dimensional changes with pressure. Comparing the resulting pressure dependences of the unit cell dimensions with the measured dependences of Worlton and Beyerlein[2] (Table 3), we estimate that errors in the elastic constant data introduced by assuming constant compressibilities are <0.1% at 8.9 kbar.

Some transit time data could be obtained in the high pressure phase (modes 2, 3, 4 and 6). Because of domain formation, it was difficult to evaluate elastic constants from transit time measurements in this phase. The data were reduced assuming the same constant compressibilities as were used for the low pressure phase; thus, the elastic constant data shown below for the high pressure phase are not strictly accurate. These data will be discussed in more detail in Section 4(b)3.

2. Ultrasonic measurements of the soft mode. The pressure dependence of the soft acoustic mode is shown in Fig. 2. This mode, denoted as mode 4 in Table 1, is the pure shear mode propagating in the <110> direction with atomic displacements (polarization) along the <110> direction. The effective elastic constant governing the velocity of this mode is C' = ½(C<sub>11</sub> - C<sub>12</sub>), and Fig. 2 shows the reduced pressure dependence of C'. From the data it is seen that C' goes smoothly and nearly linearly to zero as the transition pressure of P<sub>0</sub> = 8.86 kbar is approached from either P < P<sub>0</sub> or P > P<sub>0</sub>. The behavior of C' in the immediate vicinity of the transition is shown in the inset of Fig. 2 and the transition pressure is determined as the intercept at C' = 0 of straight lines drawn through the measured points on either side of P<sub>0</sub>. There is an uncertainty of ~±0.01 kbar in locating this intercept because there was a range of pressure in the immediate vicinity of the transition where the ultrasonic signal was too weak to obtain data and because of a small amount of scatter in the data. There is an additional uncertainty of ~±0.1 kbar in P<sub>0</sub> because of uncertainty in the absolute calibration of the pressure gauge.

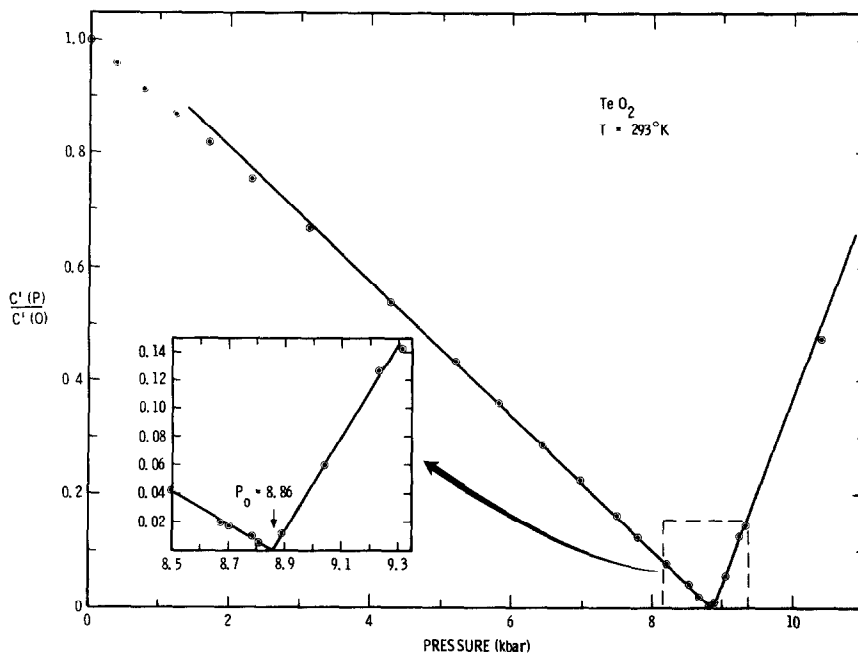


Fig. 2. Reduced elastic constant of the soft mode vs pressure. The inset shows the behavior of  $C'$  near  $P_0$ .

Data for the soft mode were obtained only for one crystal in the high pressure phase. The soft mode could not be propagated through any of our other samples in this phase. The sample for which echoes were observed in the high pressure phase gave echoes of very poor quality, especially for  $P \geq 11$  kbar. We suspect the difficulties in observing the soft mode in the high pressure phase were due to domain formation in this phase. Apparently the domains in the sample which yielded echoes for  $P > P_0$  were sufficiently large to allow some acoustic propagation. Unfortunately, this sample shattered during a later high pressure, low temperature experiment.

From Fig. 2 it appears that the pressure dependence of  $C'$  is nearly linear near the phase transition and the ratio of the slopes above and below the transition is 3:1. It is of interest to investigate if  $C'(P)$  deviates from a linear dependence near the transition which would indicate that the transition could not be described by a classical or mean-field theory. Since  $C'$  is the generalized inverse susceptibility for the transition, we can write the expected power law behavior of  $C'$  near  $P_0$  as

$$C'(P - P_0) \propto \begin{cases} (P_0 - P)^\gamma & P < P_0 \\ (P - P_0)^{\gamma'} & P > P_0. \end{cases} \quad (9)$$

Double logarithmic plots of  $C'$  vs  $|P - P_0|$  are shown in Fig. 3 and the slopes of these plots yield values for  $\gamma$  and  $\gamma'$  of  $\gamma = 1.04 \pm 0.06$  and  $\gamma' = 1.0 \pm 0.1$ . Typical error bars are indicated for two points near  $P_0$ . The horizontal error bars represent both the uncertainty in determining  $P_0$  and the uncertainty in measuring  $P$ , whereas the vertical error bars represent the uncertainty in measuring the transit time near the transition. Thus, within experimental uncertainty,  $\gamma$  and  $\gamma' = 1$ , in agreement with classical theories.

Measurements of the soft mode attenuation at high pressure were very difficult and only limited success was achieved. Good, exponential echo trains were obtained at atmospheric pressure, but application of even a few kbar caused the echo patterns to become nonexponential. Furthermore, the amplitudes of the various echoes usually oscillated as a function of pressure. Measurements were made on two different crystals, with thicknesses of 1.5 and 2.5 mm, at 10 and 70 MHz. Data from two of the runs are shown in Fig. 4. These two runs were made successively at 10 and 70 MHz on the same crystal without changing either the transducer or the bond. Figure 4 shows the amplitude of the first echo plotted logarithmically as a function of pressure for the two frequencies. The 1 bar value of the attenuation is normalized to 5 db/cm which was the attenuation measured for the overall echo train. (This value was frequency independent and is undoubtedly almost entirely instrumental since the intrinsic attenuation of mode 4 at atmospheric pressure is very small [20].) Figure 4 shows that the measured attenuation increases significantly near the transition but that this increase is essentially frequency independent between 10 and 70 MHz. Similar results were obtained in other runs except that the data typically had more scatter.

The primary question concerning these attenuation data is whether the large apparent attenuation near the transition is actually due to absorptive processes in the crystal—i.e. from “critical” sound attenuation or anharmonic coupling to other phonons—or to some artifact of the experimental arrangement. It is our belief that the apparent attenuation observed near  $P_0$  is *not* due to dissipative processes in the crystal itself, because such processes usually have a strong frequency dependence and always give rise to an attenuation proportional to the sample thickness. Within the (admittedly poor) precision

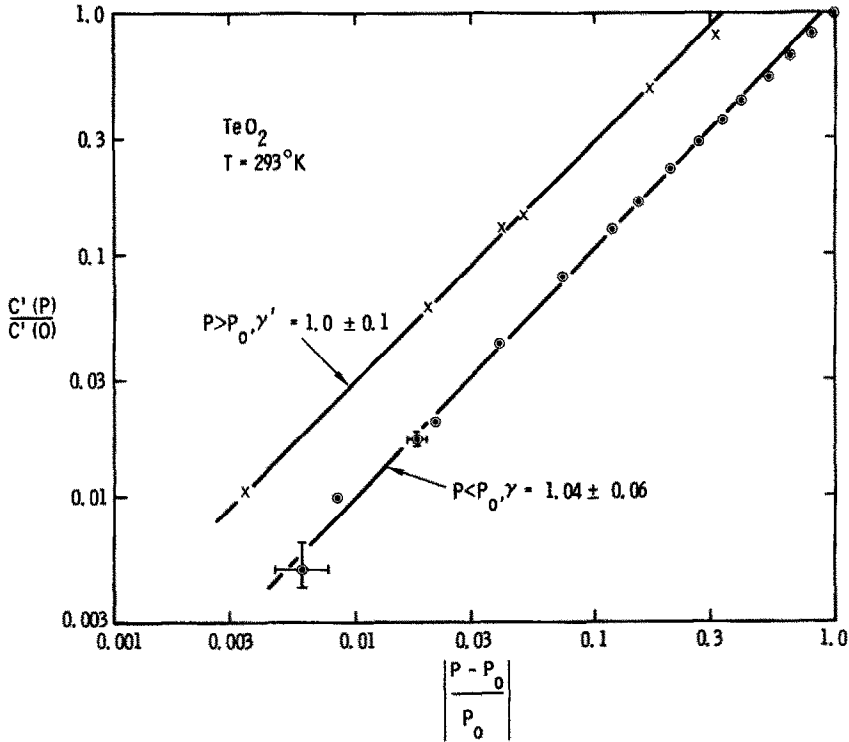


Fig. 3. Double logarithmic plots of the reduced elastic constant for the soft mode both above and below  $P_0$ .

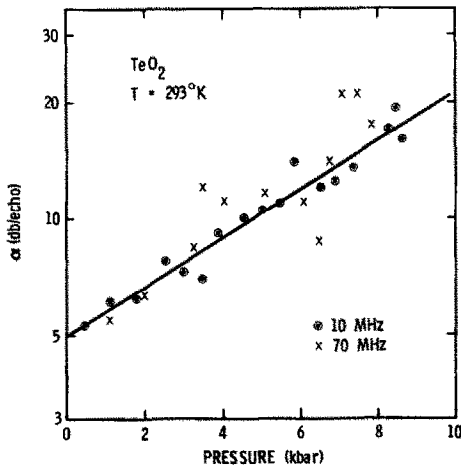


Fig. 4. Logarithmic plot of the soft mode attenuation vs pressure at 10 and 70 MHz.

of the present attenuation measurements, no such dependences were observed.

There is a simple explanation for the apparent increase in attenuation near  $P_0$  which does not depend on any dissipative process in the crystal. This explanation is based on the fact that the group velocity and the phase velocity of the acoustic wave may not be parallel [21]. A very slight deviation of the wave propagation direction  $\hat{q}$  from the  $\langle 110 \rangle$  direction can lead to a large deviation of the energy flow direction from  $\langle 110 \rangle$ . For example, assume that  $\hat{q}$  is in the  $(001)$  plane and deviates from the  $\langle 110 \rangle$  direction by a small angle  $\theta$ . Then the angle  $\Delta$  between  $\hat{q}$

and the energy flow direction is given by (see Appendix A)

$$\tan \Delta = \left( \frac{\theta}{C_{11} - C_{12}} \right) \left( \frac{2(C_{11} + C_{12})(2C_{66} + C_{12} - C_{11})}{C_{12} + C_{66}} \right). \quad (10)$$

Therefore, so long as  $\theta$  is nonzero,  $\Delta$  approaches  $90^\circ$  as  $C_{11} - C_{12}$  approaches zero. Typical numerical values are as follows: At atmospheric pressure, a misorientation of  $\theta = 0.5^\circ$  gives [20]  $\Delta = 26^\circ$ ; a misorientation of only  $0.1^\circ$  causes the energy flow to be at  $45^\circ$  to  $\hat{q}$  at a pressure of 8.5 kbar. Similar results are obtained for misorientations of  $\hat{q}$  out of the  $(001)$  plane.

In the present experiments,  $\Delta \geq 30^\circ$  would result in a significant fraction of the acoustic energy impinging on the sidewalls of the crystal. This would produce echo trains of nonexponential character and oscillations in the echo amplitudes with pressure due to interference effects. We also note that, since the  $C_{ij}$  are frequency independent, the acoustic energy flow angle  $\Delta$  is frequency independent. Thus misorientations of only a few tenths of a degree could explain the observed attenuation data. The preceding remarks are not meant to imply that there are no intrinsic dissipative processes for the soft mode, but merely that none were detected in the present measurements.

3. *Pressure dependences of the other elastic constants.* The pressure dependences of the elastic constants  $C_{11}$ ,  $C_{33}$ ,  $C_{44}$  and  $C_{66}$  are shown in Fig. 5. These curves are normalized to the 1 bar values of Ohmachi and Uchida [9] given in Table 2. All of the elastic constants except  $C_{44}$  display normal increases with pressure in the

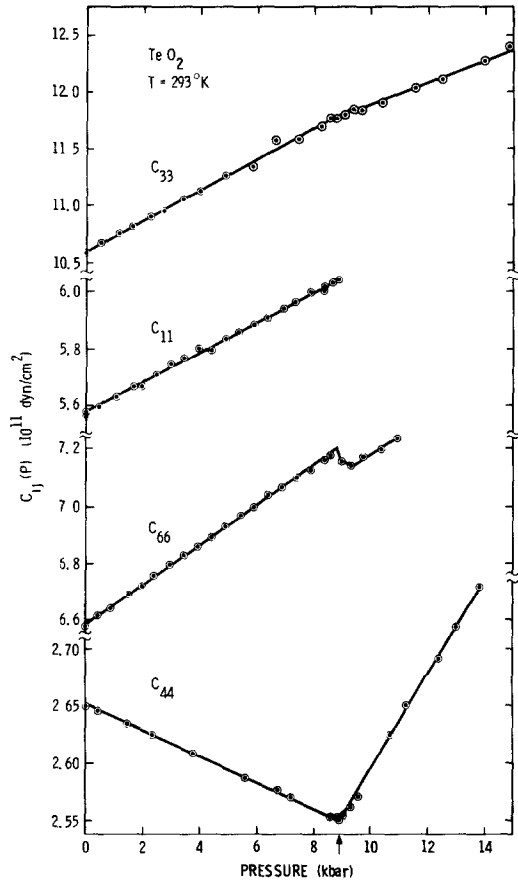


Fig. 5. Pressure dependences of various elastic constants in TeO<sub>2</sub> at room temperature.

low pressure phase; *C*<sub>44</sub> exhibits a small linear softening with pressure in this phase. The pressure derivatives for the *C*<sub>*ij*</sub> in the low pressure phase are listed in Table 4.

Table 4. Pressure dependences of the elastic constants for paratellurite in the tetragonal phase from ultrasonic and Brillouin scattering measurements

<i>c</i> <sub><i>ij</i></sub>	$\frac{d \ln c_{ij}}{dP}$ (%/kbar) (ultrasonic)	$\frac{d \ln c_{ij}}{dP}$ (%/kbar) (Brillouin)
<i>c</i> <sub>11</sub>	0.93	0.95
<i>c</i> <sub>33</sub>	1.27	1.27
<i>c</i> <sub>44</sub>	-0.42	-0.39
<i>c</i> <sub>66</sub>	1.07	1.04
<i>c</i> <sub>12</sub>		2.03 <sup>†</sup>

<sup>†</sup>Inferred from *P*<sub>0</sub>; see Sec. IV C.3.

In the high pressure phase, ultrasonic signals of good quality were obtained only for mode 6 (*C*<sub>33</sub>) and modes 3, 5 and 7 (*C*<sub>44</sub> in the low pressure phase). In fact, the quality of the signals for these modes did not change noticeably on going through the transition. Mode 2 (*C*<sub>66</sub>) gave poor quality echoes above *P*<sub>0</sub> and only limited data could be

<sup>†</sup>In particular, there is a small discontinuity in  $(d/dP)[(a + b)/2]$  at the transition.

obtained in the high pressure phase; no reliable data could be obtained in the high pressure phase for mode 1 (*C*<sub>11</sub> in the low pressure phase). It should be reemphasized that the results shown in Fig. 5 for *P* > 8.9 kbar are not strictly plots of *C*<sub>*ij*</sub> vs *P* for two reasons—the dimensional changes for the multidomained sample have not been properly taken into account, and the elastic constant tensor has lower symmetry in the high pressure phase. Since the sample breaks into domains in the high pressure phase, a measured mode velocity may be determined by an effective elastic constant which is some weighted average of the single crystal constants.

We estimate the sample dimensional changes calculated assuming constant compressibilities to be accurate to ±0.1%, although any curvature due to nonlinear pressure dependences of the unit cell dimensions is smoothed out.<sup>†</sup> [For modes propagating in a <100> or <110> direction, the changes in the acoustic path length are proportional to  $\frac{1}{2}(a + b)$  (where *a* = <100> and *b* = <010>) provided that the crystal breaks into an equal number of “positive” and “negative” domains; it is only under this provision that the constant compressibility assumption is a reasonable approximation.]

Mode 6 is determined by a single elastic constant (*C*<sub>33</sub>) in the high pressure phase and Fig. 5 indicates that there is a change in the slope of *C*<sub>33</sub> at the transition. The data also indicate that *C*<sub>33</sub> may have some curvature in the high pressure phase. Modes 3, 5 and 7 are determined by a



combination of  $C_{44}$  and  $C_{55}$ . The splitting between  $C_{44}$  and  $C_{55}$  is evidently small since good echo trains were observed in the high pressure phase. This mode increases linearly with pressure above  $P_0$  and the slope of  $C_{44}$  appears to change discontinuously at the transition. Mode 3 is determined by  $C_{66}$  in the high pressure phase and the data in Fig. 5 show that  $C_{66}$  either changes rapidly or is discontinuous at the transition; however the data for this mode are somewhat uncertain because of poor signal quality above the phase transition.

(c) Light scattering results

1. *Pressure dependence of the Raman-active optic modes.* As we noted above (Section 2(a)) all of the optic modes in TeO<sub>2</sub> are either Raman or i.r.-active at  $q \approx 0$ , with modes of  $E$  symmetry being both Raman and i.r.-active. Previous measurements [6–8] of the Raman and i.r. spectra have identified all of the optic modes except one mode of  $A_1$  symmetry. These measurements also indicated that each of the optic modes displays a normal frequency increase with decreasing temperature with the exception of a  $B_2$  mode at  $287\text{ cm}^{-1}$  and an  $E_{L0}$  mode at  $415\text{ cm}^{-1}$ . These two modes exhibit very small frequency decreases with decreasing temperature:  $(d\ln \omega(B_2)/dT) \approx +1.0 \times 10^{-4}/^\circ\text{K}$  and  $d\ln \omega(E_{L0})/dT \approx 0.3 \times 10^{-4}/^\circ\text{K}$  [6].

The present measurements of the pressure dependences of the Raman-active optic modes demonstrate that all of the observed modes display a normal frequency increase with increasing pressure throughout the low pressure tetragonal phase, and all modes have linear pressure dependences within experimental uncertainty. The mode Grüneisen parameters  $\gamma_i$  defined by

$$\gamma_i = \left( \frac{\partial \ln \omega_i}{\partial \ln V} \right)_T = \frac{1}{\kappa_V} \left( \frac{\partial \ln \omega_i}{\partial P} \right)_T \tag{11}$$

are listed in Table 5. It can be seen from Table 5 that all of the Raman-active modes display small pressure dependences with  $\gamma_i$  ranging from  $\sim 0.1$  to  $\sim 2.0$ . No soft Raman-active mode was observed in the low-pressure tetragonal phase. It should also be noted that if the transition were driven by a soft optic mode, the optic mode is expected to have  $B_1$  symmetry in the tetragonal

phase; all of the  $B_1$  modes were observed and all displayed normal pressure dependences.

Because of the 10 kbar limit of our optical pressure cell, measurements of the Raman spectra only cover a range of  $\sim 1$  kbar into the high pressure (orthorhombic) phase. These measurements are therefore insufficient for detailed examination of the pressure dependences of the Raman-active modes in the high pressure phase. Since  $\Delta P = P - P_0$  is small, the orthorhombic distortion has not evolved sufficiently for us to investigate either the splittings of the  $E$  modes (which are two-fold degenerate in the tetragonal phase) or the expected changes in symmetry of the optic modes. However,  $\Delta P$  was sufficient for us to search for any soft-optic mode above  $P_0$ ; no soft-optic mode was observed in either phase.

2. *Pressure dependences of the elastic constants from Brillouin scattering.* The pressure dependences of the elastic constants were also determined in the high frequency (hypersonic) regime using Brillouin scattering. Conservation of energy and wave vector yield a relation between the Brillouin frequency  $\omega$  and the sound velocity  $V$  of the form [22]

$$\omega = (\omega_0 V/c)(n_i^2 + n_s^2 - 2n_i n_s \cos \theta)^{1/2} \tag{12}$$

where  $\omega_0$  is the laser frequency,  $c$  is the velocity of light in a vacuum,  $\theta$  is the scattering angle and  $n_i$  ( $n_s$ ) is the refractive index for the incident (scattered) light. Paratellurite is optically active and birefringent and the refractive indices have previously been measured [23, 24]. The Brillouin data were analyzed using the values reported by Singh *et al.* [24] at 4880  $n_o = 2.3297$  and  $n_e = 2.4951$ . These values were obtained at atmospheric pressure; to our knowledge, the pressure dependences of  $n_o$  and  $n_e$  have not been measured for paratellurite.

The cross sections and selection rules for Brillouin scattering with  $\hat{q}$  along sufficient principal crystallographic directions to determine all of the elastic constants have been tabulated for various crystal classes by Vacher and Boyer [22]. This tabulation includes the propagation directions and polarizations for the incident and scattered light. Since the 422 symmetry class to which paratellurite belongs in the low pressure phase is included in their

Table 5. Pressure dependences and mode Grüneisen parameters for the Raman-active modes in the tetragonal phase of paratellurite at 295°K

Symmetry	$\omega_i$ ( $\text{cm}^{-1}$ )	$d\ln \omega_i/dP$ (%/kbar)	$\gamma_i$	Symmetry	$\omega_i$ ( $\text{cm}^{-1}$ )	$d\ln \omega_i/dP$ (%/kbar)	$\gamma_i$
$A_1$	148	0.24	1.1	$B_2$	155	0.10	0.5
$A_1$	393	0.13	0.6	$B_2$	288	0.13	0.6
$A_1$	648	0.04	0.2	$B_2$	414	0.07	0.3
$B_1$	62	0.29	1.3	$B_2$	782	$\sim 0.02$	0.1
$B_1$	175	0.18	0.8	$E$	122	0.23	1.0
$B_1$	216	0.17	0.8	$E$	197	0.16	0.7
$B_1$	232	0.17	0.8	$E$	337	0.16	0.7
$B_1$	592	$\sim 0.02$	$\sim 0.1$	$E$	718	0.04	0.2
				$E$	808	0.03	0.1

tabulation, we will not enumerate the selection rules here, but will only indicate the propagation directions and polarizations used in the present measurements. These quantities are given in Table 6.

The procedure for evaluating the pressure derivatives of the elastic constants from Brillouin measurements is illustrated below. For the case of a medium with an isotropic refractive index and in the approximation of  $n_i = n_s = n$ , eqn (12) becomes

$$\omega = (2\omega_0 Vn/c) \sin \theta/2. \quad (13)$$

Thus, the pressure dependence of  $\omega$  at constant  $\theta$  contains the pressure dependence of the density and refractive index as well as the pressure dependence of the effective elastic constant  $C^*$ . When these quantities are taken into consideration, one obtains an expression for  $\partial \ln C^*/\partial P$  of the form

$$\partial \ln C^*/\partial P = 2\partial \ln \omega/\partial P + \kappa_V - 2\partial \ln(n)/\partial P. \quad (14)$$

Knowledge of  $\kappa_V$  and  $\partial \ln(n)/\partial P$  therefore allows one to evaluate  $\partial \ln C^*/\partial P$  from  $\partial \ln \omega/\partial P$  through eqn (14). For the more general case where  $\omega$  is governed by eqn (12) rather than eqn (13), both  $\partial \ln(n_o)/\partial P$  and  $\partial \ln(n_e)/\partial P$  must be taken into account.

The pressure dependences of the  $C_{ij}$  obtained from Brillouin scattering using the procedure described above are compared with the corresponding pressure dependences measured by ultrasonic techniques in Table 4. As we indicated above, the pressure dependences of  $n_o$  and  $n_e$  have not been measured; however, these derivatives were estimated from the photoelastic constants (Appendix B). Since the contributions to  $\partial \ln \omega/\partial P$  from  $\partial \ln(n_i)/\partial P$  are small the uncertainties in evaluating  $\partial \ln C_{ij}/\partial P$  using estimates of  $\partial \ln(n_i)/\partial P$  obtained from the photoelastic constants are probably negligible. The agreement between the values of  $\partial \ln C_{ij}/\partial P$  obtained by the two techniques (Table 4) indicates this to be the case; however, we feel that the pressure derivatives determined by ultrasonic techniques are more accurate than those evaluated from Brillouin scattering measurements.

Because of the uncertainty in the pressure dependences of  $n_o$  and  $n_e$ , as well as the expected changes in  $n_i$  at the phase transition when the crystal structure changes from tetragonal to orthorhombic, Brillouin scattering was not used for detailed examination of the changes in the  $C_{ij}$  at the phase transition or in the high pressure phase. The pressure dependence of the soft mode was examined by Brillouin scattering, however, and the results are discussed in Section 4(c) 3.

Table 6. Phonon propagation directions  $\hat{q}$ , light propagation directions  $\hat{k}_i$  and polarizations  $\hat{e}_i$  used to measure the various elastic constants by Brillouin scattering

$C_{ij}$	$\hat{q}$	$\hat{k}_i$	$\hat{k}_s$	$\hat{e}_i$	$\hat{e}_s$
$C_{11}$	$\langle 100 \rangle$	$\langle 110 \rangle$	$\langle \bar{1}10 \rangle$	$\langle 001 \rangle$	$\langle 001 \rangle$
$C_{33}$	$\langle 001 \rangle$	$\langle 101 \rangle$	$\langle 10\bar{1} \rangle$	$\langle 001 \rangle$	$\langle 010 \rangle$
$C_{66}$	$\langle 100 \rangle$	$\langle 101 \rangle$	$\langle \bar{1}01 \rangle$	$\langle 010 \rangle$	$\langle \bar{1}01 \rangle$

3. *Brillouin scattering from the soft mode.* For  $\hat{q}$  precisely along  $\langle 110 \rangle$  and the incident and scattered light parallel to  $\langle 100 \rangle$  and  $\langle 010 \rangle$ , the cross section for Brillouin scattering from the soft mode  $\rho V_s^2 = \frac{1}{2}(C_{11} - C_{12}) = C'$  vanishes by symmetry. To investigate this mode by Brillouin scattering, the crystal was therefore rotated about  $\langle 001 \rangle$  so that  $\hat{q}$  made a small angle  $\psi$  relative to the  $\langle 110 \rangle$  crystal axis. While this rotation yields a finite cross section for Brillouin scattering from the soft mode, it adds a small contribution to  $C'$  from the admixture of other elastic constants. Specifically, the velocity of the soft mode changes from  $\rho V_s^2 = \frac{1}{2}(C_{11} - C_{12})$  to

$$\rho V_s^2(\phi) = \{C_{11} + C_{66} - [(C_{11} - C_{66})^2 + 4 \sin^2 \phi \cos^2 \phi (C_{12}^2 - C_{11}^2 + 2C_{11}C_{66} + 2C_{12}C_{66})]^{1/2}\} \quad (15)$$

where  $\phi = \pi/4 - \psi$ . For small angles  $\psi$ , the additional contribution to  $C$  which results from this rotation is small compared to  $C'$  at atmospheric pressure. This mode could be observed for  $\psi \geq 2^\circ$  and the Brillouin frequency was found to agree with the angular dependence predicted by eqn (15). However, as  $C'$  softens with pressure, the contribution from the other elastic constants becomes appreciable and dominates the sound velocity in the vicinity of the phase transition pressure (see Fig. 6).

To evaluate the pressure dependence of  $V_s(\phi)$ , we require the pressure dependences of  $C_{11}$ ,  $C_{12}$  and  $C_{66}$ . The pressure derivatives  $d \ln C_{11}/dP$  and  $d \ln C_{66}/dP$  are given in Table 4; assuming the elastic constants vary linearly with pressure throughout the tetragonal phase and that the velocity of the soft mode vanishes at  $P_0$  (i.e.  $C_{11} = C_{12}$  at  $P_0$ ) yields  $d \ln C_{12}/dP = 2.03\%/kbar$ . Using this value for  $d \ln C_{12}/dP$  and the values for  $d \ln C_{11}/dP$  and  $d \ln C_{66}/dP$  given in Table 4, the

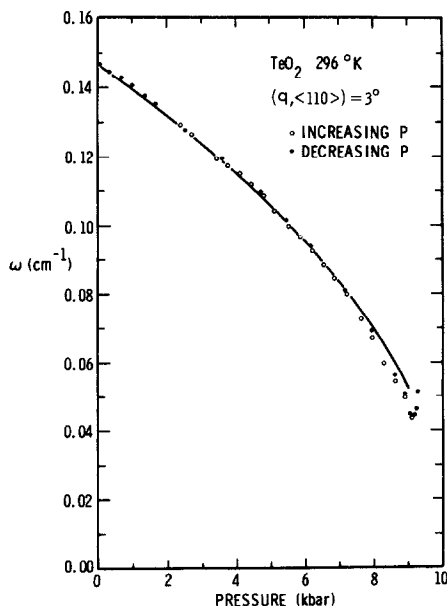


Fig. 6. Comparison between the measured and calculated pressure dependence of the soft mode Brillouin frequency for  $\hat{q}$   $3^\circ$  from  $\langle 110 \rangle$ .

pressure dependence of  $V_s(\phi)$ , can be calculated for any angle  $\psi$ . Using these values, the pressure dependence of  $\omega$  is calculated for  $\psi = 3^\circ$  and compared with the measured dependence in Fig. 6. This comparison includes the estimated changes in the refractive indices (Appendix B) and density with pressure. The agreement between the measured and predicted pressure dependence is good for pressures up to  $\sim 7$  kbar; above this pressure, the calculated pressure dependence deviates slightly from the measured value. This deviation may reflect deviations of the elastic constants from their linear pressure dependence. It may also be due in part to a small misorientation of the crystal, since a small crystal misalignment would have a large effect on  $\omega$  near the phase transition. Thus, within experimental uncertainty, the Brillouin scattering measurements indicate that the phase transition is second order, driven by the soft acoustic mode  $\rho V_s^2 = \frac{1}{2}(C_{11} - C_{12})$ .

#### (d) Dielectric properties

1. *Results of the dielectric measurements.* Figure 7 shows the variations of the static dielectric constants  $\epsilon_a$  and  $\epsilon_c$  with temperature at 1 bar. The data have been corrected for thermal expansion. Both  $\epsilon_a$  and  $\epsilon_c$  decrease smoothly with decreasing temperature and approach 0°K with zero slope, which is the normal response for ionic crystal. To our knowledge these are the only measurements on paratellurite that extend to 4°K. Ohmachi and Uchida[9] measured  $\epsilon_a$  and  $\epsilon_c$  between  $\sim 120^\circ\text{K}$  and  $430^\circ\text{K}$ . Their results are similar to ours but the absolute values of  $\epsilon_a$  and  $\epsilon_c$  are somewhat different. For example, at  $293^\circ\text{K}$  we obtain  $\epsilon_a = 22.59 \pm 0.35$  and  $\epsilon_c = 26.76 \pm 0.35$ . The major uncertainty in these values is due to uncertainties in sample dimensions. Ohmachi and Uchida's values[9] at  $293^\circ\text{K}$  are:  $\epsilon_a = 22.9 \pm 1.0$  and  $\epsilon_c = 24.7 \pm 1.5$ . Schweppe[10] reports room temperature values of  $\epsilon_a = 21.4$  and  $\epsilon_c = 24.9$ , but no details or error limits are given. The various  $\epsilon_a$  values agree within stated

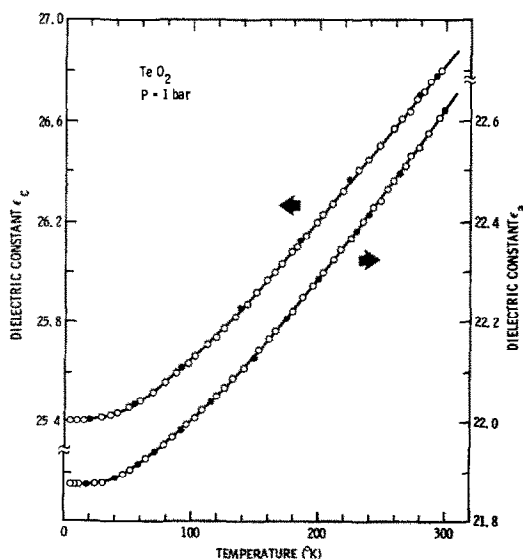


Fig. 7. Atmospheric pressure temperature dependences of  $\epsilon_a$  and  $\epsilon_c$  for TeO<sub>2</sub>.

limits, but our value of  $\epsilon_c$  is the highest value. We have no explanation for this difference, but it may be due to recent improvements in the quality of available crystals.

Figure 8 shows the pressure dependences in the low pressure phase of  $\epsilon_a$  and  $\epsilon_c$  at  $295^\circ\text{K}$  and  $75.6^\circ\text{K}$ . The data are presented as fractional changes in the dielectric constants before and after (dashed lines) correction for the dimensional changes of the samples. With the exception of our brief earlier report[1], no other pressure measurements are available. The decrease of  $\epsilon_c$  with pressure is the normal response for ionic crystals, whereas the increase in  $\epsilon_a$  with pressure is anomalous. We shall discuss the reasons for this later. Values of the corrected pressure derivatives  $(\partial \ln \epsilon_i / \partial P)_T$  at various temperatures are given in Table 7. These derivatives increase in magnitude with increasing temperature.

Figure 9 shows the pressure dependence of the reduced dielectric constants through the phase transition. The data shown are not corrected for the dimensional changes of the samples due to compression, i.e. these are the measured fractional changes in sample capacitance which are measured to better than 1 part in  $10^4$ . The data clearly show the anomaly in sample capacitance  $C_a$  associated with the transition. It is most interesting (as noted earlier[1]) that no anomaly is seen for measurements along the  $c$ -axis where  $C_c$  continues to decrease smoothly with pressure through the transition. However, this lack of  $C_c$  anomaly at the transition does not imply that there is no anomaly in  $\epsilon_c$ ; rather it may be due to the accidental cancellation of competing dimensional effects. Recall that  $C_c = \epsilon_0 \epsilon_c A / t$  where  $\epsilon_0 = 8.85 \times 10^{-12}$  farads/meter is the permittivity of free space,  $A$  ( $\propto a^2$ ) is the active area of the sample plate and  $t$  ( $\propto c$ ) is its thickness.

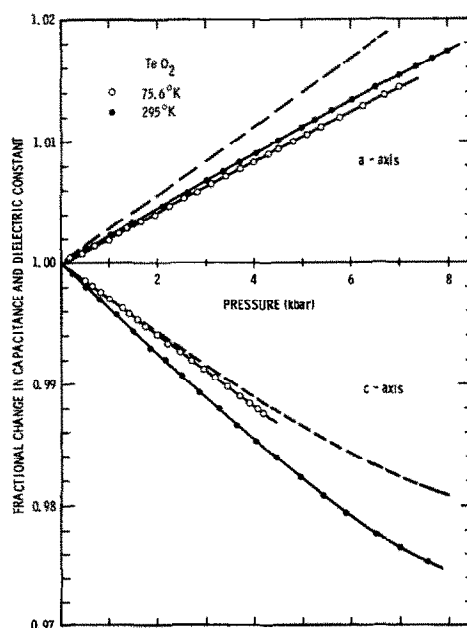


Fig. 8. Pressure dependences of  $\epsilon_a$  and  $\epsilon_c$  in the tetragonal phase at  $295^\circ\text{K}$  and  $75.6^\circ\text{K}$ . The solid lines are the measured capacitance changes whereas the dashed lines represent the actual dielectric constants at  $295^\circ\text{K}$  obtained by correcting the measured capacitance for dimensional changes of the samples.

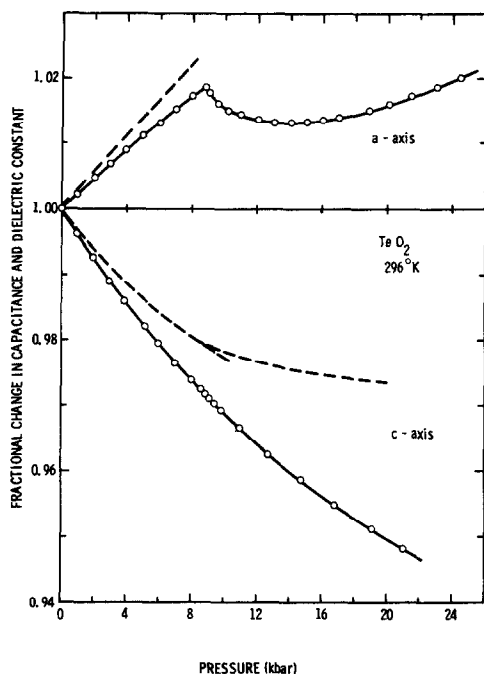


Fig. 9. Reduced pressure dependences of  $\epsilon_a$  and  $\epsilon_c$  through the phase transition. The dashed lines represent the dielectric constants obtained by correcting the measured capacitances (solid lines) for dimensional changes.

Some difficulties are encountered in determining accurately the exact details of the  $\epsilon_a$  and  $\epsilon_c$  anomalies at the transition from the  $C_a$  and  $C_c$  data. Whereas we can measure  $C_a$  and  $C_c$  with great precision through the transition, the details of the variations of the lattice parameters  $a$  and  $c$  are not well known. Worlton and Beyerlein[2] give only a few  $a(P)$  and  $c(P)$  points on

either side of the transition and the uncertainties are relatively high. In addition the transition involves a change from tetragonal to orthorhombic symmetry so that the orientation of the samples in the high pressure orthorhombic phase becomes uncertain. As a result the fractional changes in  $\epsilon_a$  and  $\epsilon_c$  shown in Fig. 9 (dashed lines) are only approximate with respect to the details of the transition and the pressure dependences of  $\epsilon_a$  and  $\epsilon_c$  in the orthorhombic phase. They were deduced from the capacitance data using the smoothed values of Worlton and Beyerlein's data given in Table 3 and the assumption that the original tetragonal  $a$  axis transforms to  $\frac{1}{2}(a+b)$  in the orthorhombic phase. The analysis then reveals the small anomaly in  $\epsilon_c$  at the transition, shown in Fig. 9.

Figure 10 shows the temperature dependence of the dielectric constant for an originally  $a$ -cut sample in the high pressure phase. These data have not been corrected for thermal expansion of the crystal, but the correction will be quite small. The behavior is normal in that  $\epsilon$  exhibits a small increase with increasing temperature. The effect is quantitatively quite comparable to that of  $\epsilon_a(T)$  of the tetragonal phase.

Results of the uniaxial stress measurements at 295°K are given in Table 7 as logarithmic derivatives of  $\epsilon_c$  with respect to  $c$ -axis stress  $\sigma_3$  and of  $\epsilon_a$  with respect to  $a$ -axis stress  $\sigma_1$ . These data show that whereas  $\epsilon_a$  increases and  $\epsilon_c$  decreases with hydrostatic pressure,  $\epsilon_a$  decreases with compression ( $-\sigma_1$ ) along  $a$  and  $\epsilon_c$  increases with compression ( $-\sigma_3$ ) along  $c$ .

2. *The magnitudes of the static dielectric constants.* The static dielectric constants of paratellurite are 4 to 5 times larger than those of normal ionic crystals and this deserves a brief comment. The static dielectric constant of an ionic crystal is determined by the sum of an electronic contribution and a lattice contribution. For a

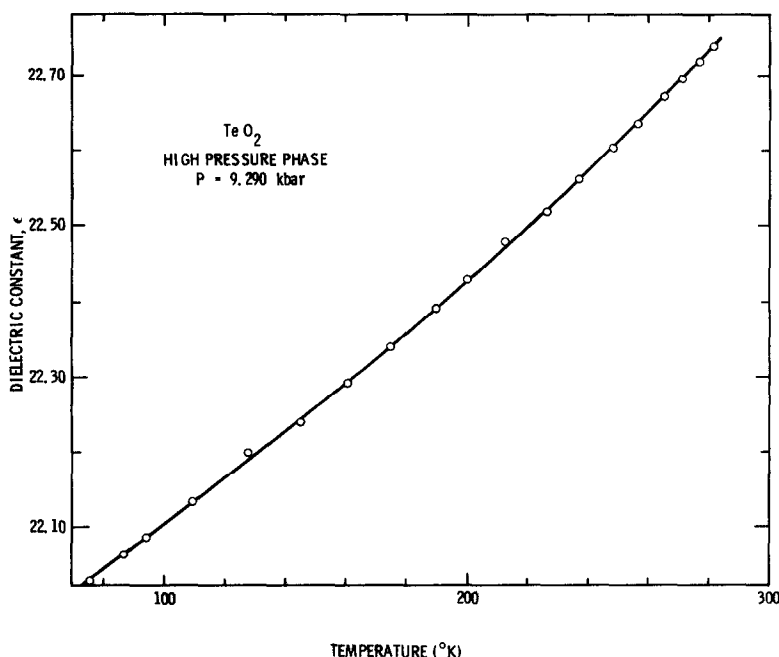


Fig. 10. Temperature dependence of  $\epsilon_a$  in the high pressure phase of  $\text{TeO}_2$ .

Table 7. Temperature and pressure dependences of the dielectric properties of TeO<sub>2</sub>; the hydrostatic pressure and uniaxial stress derivatives of  $\epsilon_{\infty,i}$  are inferred from Appendix B (Table 10)

$\psi$	$T$ (°K)	$(\partial \ln \psi / \partial T)_P$ (10 <sup>-4</sup> /°K)	$(\partial \ln \psi / \partial P)_T$ (10 <sup>-3</sup> /kbar)	$(\partial \ln \psi / \partial \sigma_1)_T$ (10 <sup>-2</sup> /kbar)	$(\partial \ln \psi / \partial \sigma_3)_T$ (10 <sup>-2</sup> /kbar)	$(\partial \ln \psi / \partial \epsilon_{na})_{c,T}$	$(\partial \ln \psi / \partial \epsilon_{na})_{a,T}$
$\epsilon_a$	75.6	0.92 ± 0.05	2.76 ± 0.1				
	295	1.42 ± 0.05	2.86 ± 0.2	1.02 ± 0.35		-7.1	14.1
	353	--	2.87 ± 0.2				
$\epsilon_c$	75.6	1.15 ± 0.06	-2.10 ± 0.1				
	295	1.97 ± 0.06	-2.66 ± 0.1		-0.11 ± 0.04	1.1	1.5
$\epsilon_{\infty,a}$	295	~0.15	1.75	-0.94	0.15	5.6	17.7
$\epsilon_{\infty,c}$	295	~0.04	1.63	0.024	0.11	-0.5	-1.3

triatomic crystal like TeO<sub>2</sub>,  $\epsilon$  is given by [25]

$$\epsilon = \epsilon_{\infty} + \frac{4\pi(Ze^*)^2}{v\omega_i^2} \left( \frac{1}{m_1} + \frac{1}{2m_2} \right) \left( \frac{\epsilon_{\infty} + 2}{3} \right)^2 = \epsilon_{\infty} + \epsilon_l \tag{16}$$

where  $\epsilon_{\infty}$  is the high frequency or optical dielectric constant ( $=n_{a,c}^2$ , where  $n$  is the appropriate refractive index in the limit of long wavelengths),  $Z$  is the valence of the Te ion,  $e^*$  is the Szigetti effective ionic charge,  $v$  is the volume per molecule,  $\omega_i$  is the appropriate resonance frequency and  $m_1$  and  $m_2$  are the masses of the Te and O ions, respectively.  $\epsilon_{\infty}$  is determined solely by the electronic polarizabilities of the Te and O ions in paratellurite. The second term on the right-hand side of eqn (16),  $\epsilon_l$ , represents the lattice contribution which is associated with the opposite (transverse) displacements of the positive Te and negative O ions for the long wavelength optical vibrations. The electronic polarizabilities of the ions influence  $\epsilon_l$  in the two different ways: first via the effective ionic charge  $e^*$ —a short-range effect—and secondly via the factor  $[(\epsilon_{\infty} + 2)/3]^2$  which arises from long-range interactions between electronic and ionic displacements.

For paratellurite the long wavelength values of  $n$  at 293°K are [24]:  $n_a = 2.1955$  and  $n_c = 2.3373$  yielding  $\epsilon_{\infty,a} = 4.82$  and  $\epsilon_{\infty,c} = 5.46$ . These are large values and are an interesting property of TeO<sub>2</sub>. The values of  $\epsilon_l$  at 293°K are then  $\epsilon_{l,a} = 17.8$  and  $\epsilon_{l,c} = 21.4$ . From eqn (16) it can be seen that large values of  $\epsilon_l$  can arise in two different ways ( $e^*$  is always  $\leq e$ , so it cannot be responsible for large  $\epsilon_l$ ): (i) an abnormally small value of  $\omega_i$  as is the case for materials with a soft optic mode, or (ii) a large value of the electronic enhancement factor  $[(\epsilon_{\infty} + 2)/3]^2$ . The i.r. measurements of Korn *et al.* [7] do not show that any of the zone center transverse optic (T0) phonons in paratellurite has a relatively small value. The  $[(\epsilon_{\infty} + 2)/3]^2$  factor on the other hand is quite large, being 5.3 and 6.25 for measurements along the  $a$  and  $c$  axes, respectively. For normal ionic crystals  $[(\epsilon_{\infty} + 2)/3]^2$  is typically  $\approx 2$ –3 (e.g. 2.1 for NaCl). Thus the large values of the  $\epsilon_l$  and thereby the  $\epsilon_l$  of paratellurite are largely determined by

the large  $\epsilon_{\infty}$ . Furthermore, if we write

$$\epsilon_l = \frac{4\pi(Ze^*)^2}{v\omega_i^2} \left( \frac{1}{m_1} + \frac{1}{2m_2} \right) \left( \frac{\epsilon_{\infty} + 2}{3} \right)^2 = A \left( \frac{\epsilon_{\infty} + 2}{3} \right)^2 \tag{17}$$

then the above values yield  $A = 3.34$  and 3.41 for the  $a$  and  $c$  axes, respectively, indicating that the anisotropy in the values of the static dielectric constants arises almost exclusively from the anisotropy of the electronic dielectric constants (or indices of refraction).

3. *Explicit dependences of  $\epsilon_{a,c}$  on temperature, volume and axial strains.* For a cubic or isotropic material the measured temperature dependence of the dielectric constant at constant pressure arises from two contributions: (i) the change which arises solely from the change in crystal volume, i.e. the explicit volume effect, and (ii) the change which would occur even if the volume of the sample were to remain fixed, i.e. the explicit, or pure temperature, effect. For a tetragonal crystal such as TeO<sub>2</sub>,  $\epsilon$  also depends on the axial ratio  $c/a$ , and the isobaric temperature dependence of  $\epsilon_i$  ( $i = a, c$ ) is given by [26]

$$\left( \frac{\partial \ln \epsilon}{\partial T} \right)_P = 2 \left( \frac{\partial \ln \epsilon}{\partial \ln a} \right)_{c,T} \left( \frac{\partial \ln a}{\partial T} \right)_P + \left( \frac{\partial \ln \epsilon}{\partial T} \right)_V + \left( \frac{\partial \ln \epsilon}{\partial \ln c} \right)_{a,T} \left( \frac{\partial \ln c}{\partial T} \right)_P \tag{18a}$$

$$= 2\beta_a \left( \frac{\partial \ln \epsilon}{\partial \ln a} \right)_{c,T} + \beta_c \left( \frac{\partial \ln \epsilon}{\partial \ln c} \right)_{a,T} + \left( \frac{\partial \ln \epsilon}{\partial T} \right)_V \tag{18b}$$

Equation (18) can be recast in the form of the expression appropriate for an isotropic crystal, namely

$$\left( \frac{\partial \ln \epsilon}{\partial T} \right)_P = -\frac{\beta_V}{\kappa_V} \left( \frac{\partial \ln \epsilon}{\partial P} \right)_T + \left( \frac{\partial \ln \epsilon}{\partial T} \right)_V + \alpha, \tag{19}$$

where

$$\alpha = \frac{2(\beta_a \kappa_c - \beta_c \kappa_a)}{\kappa_V} \left[ \left( \frac{\partial \ln \epsilon}{\partial \ln a} \right)_{c,T} - \left( \frac{\partial \ln \epsilon}{\partial \ln c} \right)_{a,T} \right] \tag{20}$$

corrects the isotropic equation for the  $c/a$  dependence. Isobaric temperature and isothermal hydrostatic pressure measurements alone are therefore not sufficient to evaluate the pure temperature contributions to the isobaric temperature derivatives of the dielectric constants. One also needs the strain dependences of the  $\epsilon_i$  determined from uniaxial stress measurements. One can show that for the  $D_4$  symmetry of  $\text{TeO}_2$  the following expressions obtain for  $\epsilon$  [27]:

$$\left(\frac{\partial \ln \epsilon}{\partial \sigma_3}\right)_T = -2s_{13} \left(\frac{\partial \ln \epsilon}{\partial \ln a}\right)_{c,T} - s_{33} \left(\frac{\partial \ln \epsilon}{\partial \ln c}\right)_{a,T} \tag{21}$$

$$\left(\frac{\partial \ln \epsilon}{\partial \sigma_1}\right)_T = -(s_{11} + s_{12}) \left(\frac{\partial \ln \epsilon}{\partial \ln a}\right)_{c,T} - s_{13} \left(\frac{\partial \ln \epsilon}{\partial \ln c}\right)_{a,T} \tag{22}$$

$$\begin{aligned} \left(\frac{\partial \ln \epsilon}{\partial P}\right)_T = & -2(s_{11} + s_{12} + s_{13}) \left(\frac{\partial \ln \epsilon}{\partial \ln a}\right)_{c,T} - (s_{33} + 2s_{13}) \\ & \times \left(\frac{\partial \ln \epsilon}{\partial \ln c}\right)_{a,T} \end{aligned} \tag{23}$$

where the  $s_{ij}$  are the elastic compliances, and  $-\sigma_1$  and  $-\sigma_3$  are the uniaxial compressive stresses along the  $a$  and  $c$  axes, respectively. Values used for the  $s_{ij}$ ,  $\kappa_i$  and  $\beta_i$  are given in Table 2.

The different contributions to the isobaric temperature dependence of the  $\epsilon_i$  are summarized in Table 8. The terms  $2\beta_a(\partial \ln \psi / \partial \ln a)_{c,T}$  and  $\beta_c(\partial \ln \psi / \partial \ln c)_{a,T}$  represent the contributions to  $(\partial \ln \epsilon_i / \partial T)_P$  from changes in the volume and  $c/a$  ratio with temperature. The contribution to  $\epsilon_a(T)$  from dimensional changes with temperature is appreciably larger than the corresponding contribution to  $\epsilon_c(T)$ , and  $(\partial \ln \epsilon_a / \partial \ln a)_{c,T}$  is negative and thus anomalous. We also note that the contribution to  $\epsilon_a$  from changes in  $c/a$ , contained in  $\alpha$ , are appreciably larger than the pure-volume contribution, whereas the opposite behavior holds for  $\epsilon_c$ . However, the results of Table 8 show that the isobaric temperature dependences

of both  $\epsilon_a$  and  $\epsilon_c$  are dominated by the pure temperature effect  $(\partial \ln \epsilon_i / \partial T)_V$  which arises from higher-order anharmonicities.

An analysis of the contributions to the isothermal pressure derivatives is shown in Table 9. As in the case of the isobaric temperature dependences, the individual axial contributions are large and have opposite signs for  $\epsilon_a$  whereas  $\epsilon_c$  is composed of smaller  $a$ - and  $c$ -axis contributions of the same sign.

The decrease of  $\epsilon_c$  with pressure is the normal behavior for ionic crystals—the decrease in polarizability with decreasing unit cell volume (the lattice gets stiffer) more than compensates for the increase in the density of polarizable molecules (an effect that would cause  $\epsilon$  to increase). The increase in  $\epsilon_a$  with pressure is anomalous. This increase is 0.29%/kbar at 295°K as compared with an increase in density of 0.22%/kbar. As seen from Table 9,  $\epsilon_a$  increases with pressure because of the  $a$ -axis strain contribution.

4. *Pressure and temperature dependences of the optical dielectric constants.* The optical dielectric constants ( $\epsilon_{\omega,i} = n_i^2$ ) of paratellurite are large and make a significant contribution to the magnitudes of the static dielectric constants  $\epsilon_i$ . Uchida [23] has reported the 1 bar temperature dependences of the refractive indices as a function of wavelength. His results display considerable wavelength dispersion in the temperature derivatives but these derivatives appear to be approaching limiting values by the long wavelength limit of his measurements (0.7  $\mu$ ). Table 7 gives  $(\partial \ln \epsilon_{\omega,i} / \partial T)_P = 2(\partial \ln (n_i) / \partial T)_P$  at 0.7  $\mu$ ; Table 10 gives the hydrostatic and uniaxial stress derivatives of  $\epsilon_{\omega,i}$  which were evaluated from the photoelastic constant measurements (Appendix B).

The results in Tables 7 and 10 indicate that  $\epsilon_{\omega,a}$  and  $\epsilon_{\omega,c}$  increase with both increasing temperature and pressure. The temperature dependences of the  $\epsilon_{\omega,i}$  are anomalous since the typical behavior for ionic crystals is for  $n_i$  (and

Table 8. Isobaric temperature derivatives of  $\epsilon_i$  expressed in terms of dimensional and pure temperature contributions at 295°K

$\psi$	$(\partial \ln \psi / \partial T)_P$ ( $10^{-4}/^\circ\text{K}$ )	$=$	$2\beta_a(\partial \ln \psi / \partial \ln a)_{c,T}$ ( $10^{-4}/^\circ\text{K}$ )	$+$	$\beta_c(\partial \ln \psi / \partial \ln c)_{a,T}$ ( $10^{-4}/^\circ\text{K}$ )	$+$	$(\partial \ln \psi / \partial T)_{c,a}$ ( $10^{-4}/^\circ\text{K}$ )	$-$	$\frac{\beta_a}{\alpha_a}(\partial \ln \psi / \partial P)_T$ ( $10^{-4}/^\circ\text{K}$ )	$\alpha_i$ ( $10^{-4}/^\circ\text{K}$ )
$\epsilon_a$	1.42	$=$	-2.83		+0.93		+ 3.32		- 0.60	- 1.30
$\epsilon_c$	1.97	$=$	+0.43		+0.10		+ 1.44		0.56	- 0.03
$\epsilon_{\omega,a}$	~0.15	$=$	2.22		-1.17		- 0.90		- 0.36	+ 1.42
$\epsilon_{\omega,c}$	~0.04	$=$	-0.20		-0.09		+ 0.33		- 0.34	+ 0.05

Table 9. Axial contributions to the pressure dependences of  $\epsilon_i$  at 295°K

$\psi$	$(\partial \ln \psi / \partial P)_T$ ( $10^{-3}/\text{kbar}$ )	$=$	$-2\kappa_a(\partial \ln \psi / \partial \ln a)_{c,T}$ ( $10^{-3}/\text{kbar}$ )	$-$	$\kappa_c(\partial \ln \psi / \partial \ln c)_{a,T}$ ( $10^{-3}/\text{kbar}$ )
$\epsilon_a$	2.86	$=$	+ 11.48		- 8.62
$\epsilon_c$	-2.66	$=$	- 1.74		- 0.92
$\epsilon_{\omega,a}$	1.75	$=$	- 9.1		+10.8
$\epsilon_{\omega,c}$	1.63	$=$	+ 0.8		+ 0.8

Table 10. Hydrostatic pressure and uniaxial stress derivatives of the refractive indices of TeO<sub>2</sub> determined from the photoelastic constants

(μ)	$n_1$ (a)	$(\partial \ln n_1 / \partial P)_T$ (10 <sup>-4</sup> /kbar)	$(\partial \ln n_1 / \partial \sigma_1)_T$ (10 <sup>-4</sup> /kbar)	$(\partial \ln n_1 / \partial \sigma_3)_T$ (10 <sup>-4</sup> /kbar)
0.488	$n_o = 2.3297$	9.88		
0.488	$n_e = 2.4951$	9.28		
1.152	$n_o = 2.1955$	8.77	-46.9 ( $n_1$ ) <sup>b</sup> 48.2 ( $n_2$ ) <sup>b</sup>	7.47 ( $n_1 = n_2$ )
1.152	$n_e = 2.3373$	8.14	1.21 ( $n_3$ )	5.71 ( $n_3$ )

a.) Ref. 25

b.) Note that with stress along the a-axis the crystal becomes biaxial.

therefore  $\epsilon_{\infty,i}$ ) to scale with density. The origin of this anomalous temperature dependence can be understood by examining the uniaxial stress dependence of the  $n_i$  given in Table 10. Using the results of Table 10 in conjunction with eqns (18) and eqns (21)–(23) with  $\epsilon_i$  replaced by  $\epsilon_{\infty,i}$  one can evaluate the various contributions to  $(\partial \ln \epsilon_{\infty,i} / \partial T)_P$ . The results are shown in Table 8.

These results indicate that all of the uniaxial stress derivatives of  $\epsilon_{\infty,i}$  are positive except  $(\partial \ln \epsilon_{\infty,a} / \partial \sigma_1)$  which is negative and large ( $\approx -1\%/kbar$ ). The fractional changes in  $\epsilon_{\infty,a}$  are about an order of magnitude larger than the fractional changes in  $\epsilon_{\infty,c}$ ; furthermore the change of  $\epsilon_{\infty,a}$  with  $c$ -axis strain is negative and by far the largest effect—namely  $(\partial \ln \epsilon_{\infty,a} / \partial \ln c)_{a,T} = -17.88$ . This is the quantity which dominates and determines the positive value of  $(\partial \ln \epsilon_{\infty,a} / \partial P)_T$  (see Table 9). The change of  $\epsilon_{\infty,a}$  with  $a$ -axis strain  $(\partial \ln \epsilon_{\infty,a} / \partial \ln a)_{c,T}$  is positive and thus anomalous. It results in a negative contribution to  $(\partial \ln \epsilon_a / \partial P)_T$ , and it is responsible for the anomalous increase in  $\epsilon_{\infty,a}$  (and  $n_a$ ) with temperature at 1 bar (cf. Table 7). For  $\epsilon_{\infty,c}$  on the other hand, both  $a$ - and  $c$ -axis strains lead to normal negative contributions to  $(\partial \ln \epsilon_{\infty,c} / \partial T)_P$  and the anomalous observed positive value of this derivative is determined by the pure temperature effect  $(\partial \ln \epsilon_{\infty,c} / \partial T)_{c,a}$ . The pure temperature effect for  $\epsilon_{\infty,a}$  is opposite in sign and larger in magnitude than that for  $\epsilon_{\infty,c}$ , but for  $\epsilon_{\infty,a}(T)$  the strain contributions dominate.

5. *Relation between the dielectric constants and optical phonons.* In ionic crystals the lattice contribution to the static dielectric constant arises from the long wavelength polar displacements of the positive and negative ions, i.e. the zone-center i.r.-active modes. Paratellurite has 4 i.r.-active modes with  $c$ -axis polarization ( $A_2$  modes) and 8 i.r.-active modes with  $a$ -axis polarization ( $E$  modes). These relate to  $\epsilon_c$  and  $\epsilon_a$ , respectively. In the absence of damping the dielectric constant is given by:

$$\epsilon(\omega) = \epsilon_{\infty} + \sum_j \frac{f_j}{1 - (\omega/\omega_{T0,j})^2}, \quad (24)$$

so that for the static dielectric constant (i.e.  $\omega \approx 0$ ) the lattice contribution to  $\epsilon$  is

$$\epsilon_l = \epsilon(0) - \epsilon_{\infty} = \sum_{j=1}^N f_j \quad (25)$$

where the  $f_j$  are the mode oscillator strengths and the summation is over the appropriate  $N$  modes for the different crystal orientations. Korn *et al.* [7] have recently measured the frequencies and oscillator strengths of the i.r.-active modes of paratellurite from reflectivity measurements. Their results at 295°K are:  $\sum_{j=1}^8 f_{E,j} = 18.15$

compared with our value of  $\epsilon_{l,a} = 17.72$ ; and  $\sum_{j=1}^4 f_{A2,j} = 22.28$  compared with our value of  $\epsilon_{l,c} = 21.23$ . The agreement is fairly good and within experimental error in both cases. It is considerably better than that obtained by Korn *et al.* [7] based on the earlier and less accurate values of the dielectric constants.

In the absence of damping, the dielectric constants are also related to the zone-center longitudinal ( $L0$ ) and transverse ( $T0$ ) optic phonons by the generalized Lyddane–Sachs–Teller relation

$$\frac{\epsilon}{\epsilon_{\infty}} = \prod_j \left( \frac{\omega_{L0,j}}{\omega_{T0,j}} \right)^2, \quad (26)$$

where the product is over the appropriate  $N$  modes for the particular crystal orientation. Again using Korn *et al.*'s [7] values of the 295°K i.r. frequencies, we get  $\epsilon_a/\epsilon_{\infty,a} = 4.52$  compared with our value of 4.64, and  $\epsilon_c/\epsilon_{\infty,c} = 4.78$  compared with our value of 4.84. Again the agreements are quite good.

#### The effective ionic charges

In an ideal ionic crystal consisting of deformable ions which do not overlap the individual ions can be expected to carry their formal charges given by the product of the valence  $Z$  and the electronic charge  $e$ . In real crystals, however, the ions overlap, and the concept of an effective charge  $e^*$  was introduced [25, 28] to account for the polarization effects associated with this overlap. Deviations of  $e^*/e$  from unity arise from two effects: (i) short-range repulsive interactions between the electron clouds on adjacent ions which modify the electronic dipole moments, and (ii) redistribution of charge and overlap when the ions move in the course of lattice vibrations. In principle then there should be a different effective charge associated with each mode of vibration. It should also be noted that various forms of the

expressions for  $e^*$  are in use[29, 30]; however, most generally  $e^*$  is calculated from the Szigetti relation[25] given by eqn (16) above. We emphasize that this is a "transverse" effective charge in that it relates to transverse modes.

Values for the zone center, polar  $T0$  phonons of paratellurite are available only at 295°K and we calculate the Szigetti effective charges at this temperature. Taking  $Z = 4$  and  $v = 44.0 \text{ \AA}^3$  ( $=\frac{1}{4}$  unit cell volume) along with the lowest  $T0$  mode frequencies, namely  $\omega_{T0,E} = 121 \text{ cm}^{-1}$  and  $\omega_{T0,A_2} = 82 \text{ cm}^{-1}$ , we obtain for the ratio of the effective charge  $e^*$  to the electronic charge  $e$  ( $=4.8 \times 10^{-10}$  esu) the following values:  $(e^*/e)_a = 0.27$  and  $(e^*/e)_c = 0.18$  for the  $a$ -axis and  $c$ -axis responses, respectively. These are rather small values. In highly ionic crystals the Szigetti effective charge is found to be 10–20% less than  $e$ . The possibility thus exists that the bonding in paratellurite is highly covalent. This is not inconsistent with the highly distorted rutile-type crystal structure of the material in which each Te atom is surrounded by six, unequally distant, oxygen atoms. Two of the oxygens are at a distance of 1.91 Å, two at 2.09 Å and two at 2.89 Å[5].

The question also arises: Is eqn (16) *strictly* valid for a noncentro-symmetric crystal such as paratellurite? The answer is most likely not. Equation (16) is based on the Lorentz value of the local field, namely  $E_{loc} = E + (4\pi/3)P$ , which is strictly valid only for a cubic or isotropic crystal. It is this form of the local field which leads to the  $[(\epsilon_\infty + 2)/3]^2$  term in eqn (16), thus making eqn (16) model dependent. To avoid this difficulty, one can, following Born and Huang[31], define a macroscopic transverse effective charge  $e_T^*$  given by

$$\epsilon = \epsilon_\infty + \frac{4\pi(Ze_T^*)^2}{v\omega_T^2} \left( \frac{1}{m_1} + \frac{1}{2m_2} \right) \quad (27)$$

which is not model dependent. Comparison with eqn (16) shows that  $e_T^*$  is related to the Szigetti charge  $e^*$  by

$$e_T^* = \left( \frac{\epsilon_\infty + 2}{3} \right) e^*. \quad (28)$$

For  $\text{TeO}_2$  we then find  $e_{T,a}^* = 0.61e$  and  $e_{T,c}^* = 0.45e$ . These are also relatively small values, again suggesting that the bonding in paratellurite may be quite covalent. It is worth noting in passing that the above values of  $e^*/e$  are comparable to those obtained for many covalent crystals[30].

## 5. PROPERTIES OF THE PHASE TRANSITION

Since paratellurite is the first known example of a pure strain transition, it is of interest to examine carefully whether the transition is in fact second-order. The acoustic measurements shown in Fig. 2 indicate that the soft effective elastic constant  $C' = \frac{1}{2}(C_{11} - C_{12})$  attains a very small value near the transition. The smallest reduced value observed was  $C'(P)/C'(0) = 5 \times 10^{-3}$ . Because  $\text{TeO}_2$  is already "near" the transition at atmospheric pressure,  $C'(0)$  is small ( $C'(0) = 4.5 \times 10^{10} \text{ dyn/cm}^2$ ) and the smallest value observed for  $C'(P)$  is  $C'(P) \approx 2 \times 10^8 \text{ dyn/cm}^2$

which is about three orders of magnitude smaller than typical shear constants for ionic crystals. (For example, two other shear constants of  $\text{TeO}_2$  are  $C_{44} \approx 2.7 \times 10^{11} \text{ dyn/cm}^2$  and  $C_{66} \approx 6.6 \times 10^{11} \text{ dyn/cm}^2$ .) Examination of the insert in Fig. 2 shows that no data were obtained for  $|P - P_0| \leq 0.05 \text{ kbar}$  because of poor signal quality. Straight line fits to the data on both sides of the transition extrapolate to a zero value of  $C'(P)$  at a common pressure. Thus, within the experimental uncertainty,  $C'(P)$  appears to go smoothly to zero from both sides of the transition. There is, of course, some uncertainty in the lines drawn through the data points because the data have some scatter. Thus a small discontinuity in  $C'(P)$  at the transition would not be detected; however, any discontinuity in  $C'(P)$  must be less than  $\Delta C'(P) = 1 \times 10^8 \text{ dyn/cm}^2$ .

Another important question concerning this structural phase transition is whether the critical exponents characterizing anomalies at the transition have classical (mean-field) values or if there are deviations from classical behavior due to observable critical effects. Non-classical behavior has previously been observed for structural transitions—e.g. the 110°K transition of  $\text{SrTiO}_3$ [32]—whereas other systems—e.g. the Jahn–Teller transition in  $\text{TmVO}_4$ [33]—appear to show classical behavior. As discussed in Section 4(a) 2, double logarithmic plots of  $C'(P)$  vs  $P - P_0$  should have slopes of  $\gamma$  and  $\gamma'$  in the low and high pressure phases, respectively. Within experimental uncertainty, we find that  $\gamma$  and  $\gamma'$  have classical values of  $\gamma = \gamma' = 1$ . Unfortunately, however, there are several reasons which make it difficult to obtain definitive values for  $\gamma$  and  $\gamma'$  from the ultrasonic data. First the nondivergent background contribution to the susceptibility  $1/C'(P)$  cannot be determined because no data could be obtained "far" from the transition in either phase. The background contribution will tend to make the slopes in Fig. 3 too small, which probably accounts for the curvature in the data for  $(P_0 - P)/P > 0.3$ . Secondly, reliable data are required very near  $P_0$  to determine  $\gamma$  precisely. As can be seen from the error bars and the scatter in the data for  $|P - P_0|/P_0 < 0.01$ , the data are not precise enough to reliably determine exponents in the immediate vicinity of the transition. Thirdly, the data in the high pressure phase do not represent the fundamental soft mode velocity exactly since the propagation direction for these data is at 45° to  $a$  and  $b$  whereas the soft mode propagation direction deviates from 45° by a small angle above  $P_0$ [34]. In fact, the difference between these two propagation directions may account for the difference between the measured slope ratio for  $C'(P)$  above and below  $P_0$  ( $\sim 3:1$ ) and the classical slope ratio (2:1).

While the acoustic measurements provide the strongest evidence that the transition is ideally second-order, it is also worth noting that this conclusion is supported by our Brillouin scattering and dielectric constant measurements as well as by the neutron[2] and X-ray measurements[14]. The Brillouin data indicated that within the experimental uncertainty the transition is second-order, while the dielectric data showed the transition is completely reversible with no hysteresis. Furthermore, the dielectric anomaly observed for the  $a$ -axis dielectric constant is



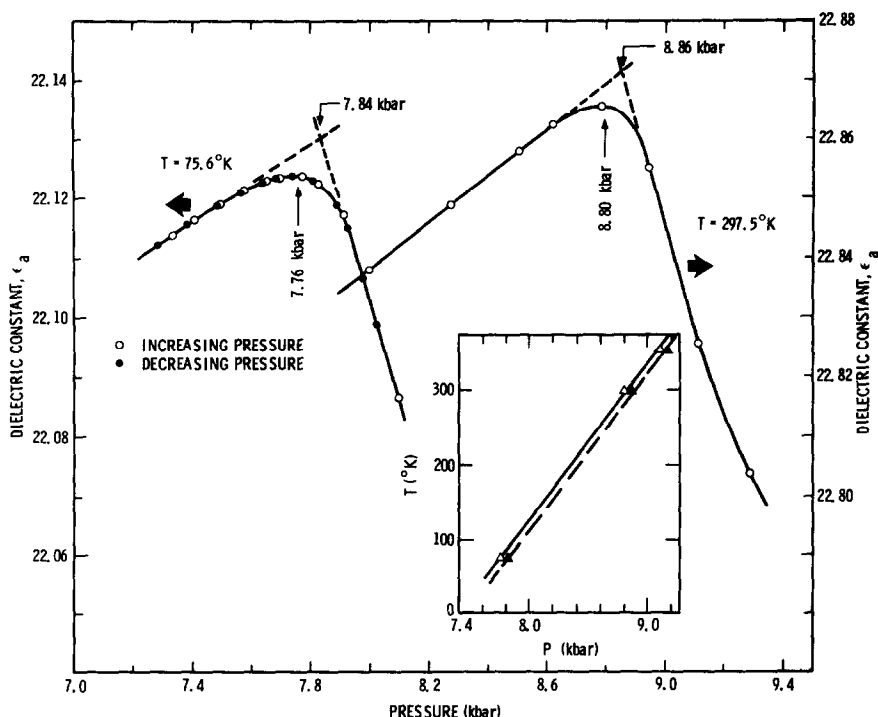


Fig. 11. Detailed behavior of  $\epsilon_a$  through the phase transition at 295 and 75.6°K. Note that there is no hysteresis associated with the transition. The inset gives the temperature dependence of the transition pressure.

small (<1%) and  $\epsilon_a$  changes smoothly through the transition with no discontinuities. The small anomaly in  $\epsilon_a$  is probably due only to structural changes associated with the transition. These features are shown for two temperatures in Fig. 11.

The inset in Fig. 11 shows the variation of the transition pressure with temperature as deduced from the  $\epsilon_a(P)$  data. Two different methods of defining the transition pressure  $P_0$  were used, as illustrated in Fig. 11. First, the location of the peak in  $\epsilon_a(P)$ , represented by the open triangles in the inset, and second the intersection of two nearly linear  $\epsilon_a(P)$  regions on either side of  $P_0$ , represented by the closed triangles in Fig. 11. As can be seen from the inset, within experimental uncertainty the temperature dependence of  $P_0$  is linear over the range covered with slope  $dP_0/dT = 4.82 \pm 0.05 \text{ bar/}^\circ\text{K}$  and is independent of the way  $P_0$  is defined. It is interesting to note, however, that the second method of defining  $P_0$ —i.e. the intersection of the two straight lines—yielded values of  $P_0$  which were in closer agreement with the values of  $P_0$  deduced from the ultrasonic data.

As indicated above, no anomaly whatsoever is observed in measurements of the  $c$ -axis capacitance so that any dielectric anomaly in  $\epsilon_c$  is sufficiently small so as to be completely cancelled by the (continuous) dimensional changes. Finally, we recall that no soft Raman-active optic mode was observed in either phase. If the transition were driven by a soft optic mode, this mode would be Raman-active in the low symmetry (high pressure) phase (Worlock's theorem)[35]. We, therefore, conclude from the Raman scattering and dielectric measurements that no optic mode is involved in the transition—i.e. the phase

transition in paratellurite is purely strain-induced and is second order within the uncertainty of our measurements.

**Acknowledgements**—The authors wish to acknowledge the expert technical assistance of J. D. Kluck, B. E. Hammons and J. E. Clickner in performing these measurements. We would also like to thank Drs. R. A. Beyerlein and T. G. Worlton for permission to use their data prior to publication, E. F. Skelton for discussions of his X-ray measurements prior to publication, J. F. Scott for bringing Ref. [3] to our attention, and W. B. Daniels for providing the design of the optical pressure cell.

#### REFERENCES

1. Percy P. S. and Fritz I. J., *Phys. Rev. Letters* **32**, 466 (1974).
2. Worlton T. G. and Beyerlein R. A. To be published.
3. Anderson P. W. and Blount E. I., *Phys. Rev. Letters* **14**, 217 (1965).
4. Fleury P. A., Lazay P. D. and Van Uitert L. G., *Phys. Rev. Letters* **33**, 492 (1974).
5. Leciejewicz J., *Z. Krist.* **116**, 345 (1961).
6. Pine A. S. and Dresselhaus G., *Phys. Rev.* **B5**, 4087 (1972).
7. Korn D. M., Pine A. S., Dresselhaus G. and Reed T. B., *Phys. Rev.* **B8**, 768 (1973).
8. Ayrault B., Decamps E., Abba F., Margueton Y. and Durand M., *Solid State Commun.* **11**, 639 (1972).
9. Ohmachi Y. and Uchida N., *J. Appl. Phys.* **41**, 2037 (1971).
10. Arlt G. and Schweppe H., *Solid State Commun.* **6**, 783 (1968); Schweppe H., *Ultrasonics* **8**, 84 (1970).
11. Hutson A. R. and White D. L., *J. Appl. Phys.* **33**, 40 (1962) and references therein.
12. The form in which we have written the equations is taken from Smith R. T. and Walsh F. S., *J. Appl. Phys.* **42**, 2219 (1971).
13. Jona J. and Shirane G., *Ferroelectric Crystals* Chapt. 3. Pergamon Press, New York (1962).
14. Garland C. W. and Novotny D. B., *Phys. Rev.* **177**, 971 (1969).
15. Skelton E. F., Liu C. Y. and Spain I. L., *Penn. State ACA Mtg. Paper M7* (1974).

16. Crystal Technology, Inc., Mountain View, CA 94040, U.S.A.
17. This experimental arrangement is essentially that described by Garland C. W. and Yarnell C. I., *J. Chem. Phys.* **44**, 3678 (1966).
18. Samara G. A., *J. Phys. Chem. Solids* **26**, 121 (1965).
19. W. C. Dillon and Co., Inc., Van Nuys, California, U.S.A.
20. Uchida N., *J. Appl. Phys.* **43**, 2915 (1972).
21. Ohmachi Y., Uchida N. and Nizeki N., *J. Acoust. Soc. Am.* **51**, 164 (1972).
22. Vacher R. and Boyer L., *Phys. Rev.* **B6**, 639 (1972).
23. Uchida N., *Phys. Rev.* **B4**, 3736 (1971).
24. Singh S., Bonner W. A. and Van Uitert L. G., *Phys. Letters* **38A**, 407 (1972).
25. Szigetti B., *Trans. Farad. Soc.* **45**, 155 (1949).
26. Fritz I. J., *J. Phys. Chem. Solids* **35**, 817 (1974).
27. Percy P. S., *Phys. Rev.* **B8**, 6018 (1973).
28. See e.g., Dick A. G. and Overhauser A. W., *Phys. Rev.* **112**, 90 (1958).
29. See e.g., Phillips J. C., *Rev. Mod. Phys.* **42**, 317 (1970); Lucovsky G., Martin R. and Burstein E., *Phys. Rev.* **B4**, 1367 (1971).
30. Lawaetz P., *Phys. Rev. Letters* **26**, 697 (1971).
31. Born M and Huang K., *Dynamical Theory of Crystal Lattices*. The Clarendon Press, Oxford (1954).
32. Müller K. A. and Berlinger W., *Phys. Rev. Letters* **26**, 13 (1971).
33. Melcher R. L., *Proc. 1973 Ultrasonics Symposium* p. 239. IEEE, New York (1973).
34. Fritz I. J. and Percy P. S. (unpublished).
35. Worlock J. M., in *Structural Phase Transitions and Soft Modes* (Edited by Samuelsen E. J., Andersen E. and Feder J.), p. 329. Universitetsforlaget, Oslo (1971).
36. Love A. E. H., *A Treatise on the Mathematical Theory of Elasticity*, p. 177. Dover Publications, New York (1944).
37. Waterman P. C., *Phys. Rev.* **113**, 1240 (1959).
38. McSkimin H. J., *J. Acoust. Soc. Am.* **34**, 1271 (1962).
39. Addison R. C., Auld B. A. and Wilkinson J. H., *Proc. IEEE* **55**, 68 (1967).
40. Nye J. F., *Physical Properties of Crystals*, Chapt. 8. University Press, Oxford (1964).

#### APPENDIX A

The energy flux vector  $\mathbf{P}$  associated with a general elastic excitation has been discussed by Love[36] and specialized to plane wave propagation by Waterman[37] and McSkimin[38]. For a plane wave  $\mathbf{u} = \mathbf{u}_0 \exp(i\mathbf{k} \cdot \mathbf{r})$  with velocity  $V = \omega/k$  the components of  $\mathbf{P}$  are

$$P_i = \frac{u_0^2 \omega^2}{2V} C_{ijkl} \hat{k}_j \hat{u}_{0k} \hat{u}_{0l}, \quad (\text{A1})$$

where  $\hat{k}_i$  and  $\hat{u}_{0i}$  are the direction cosines of  $\mathbf{k}$  and  $\mathbf{u}_0$ , respectively. We consider a plane (quasi-shear) wave propagating in the  $xy$  plane at a small angle  $\theta$  to a (110) direction. Solving the wave propagation problem for this mode yields the ratio  $u_{02}/u_{01}$  as

$$\frac{u_{02}}{u_{01}} = -1 + \frac{2\theta(C_{66} - C_{11})}{C_{66} + C_{12}}. \quad (\text{A2})$$

By combining eqns (A1) and (A2) one can calculate the ratio  $P_1/P_2$  and from this the direction of the energy flux vector. (It is easy to show that  $P_3 = U_3 = 0$  holds when  $k_3 = 0$ ). Defining  $\Delta$  as the angle between  $\mathbf{k}$  and  $\mathbf{P}$  we thus obtain eqn (10) of the text:

$$\tan \Delta = \left( \frac{\theta}{C_{11} - C_{12}} \right) \left( \frac{2(C_{11} + C_{12})(C_{66} + C_{12} - C_{11})}{C_{12} + C_{66}} \right). \quad (\text{A3})$$

An alternate derivation of this equation can be obtained by noting that  $\mathbf{P}$  is parallel to the group velocity vector  $\mathbf{V}_g$  which is given by [39]  $\mathbf{V}_g = \nabla_{\mathbf{k}} \omega(k)$ . From this equation we obtain

$$\tan \Delta = \frac{1}{V} \nabla_{\mathbf{k}} V = \frac{1}{V} \frac{dV}{d\theta}. \quad (\text{A4})$$

The velocity of the quasi-shear mode propagating at small  $\theta$  is given by the relation

$$\rho V^2 = \frac{1}{2} (C_{11} - C_{12}) + \theta^2 \frac{(C_{11} + C_{12})(C_{12} - C_{11} + 2C_{66})}{C_{12} + C_{66}}. \quad (\text{A5})$$

Combining eqns (A4) and (A5) again yields eqn (A3).

#### APPENDIX B

It was noted in Section 4 that the pressure dependences of the refractive indices are required to evaluate the pressure dependences of the Brillouin and dielectric measurements. No direct measurements of these pressure dependences have been reported, and the purpose of this Appendix is to evaluate the hydrostatic and uniaxial pressure derivatives of  $n_o$  and  $n_e$  from the measured photoelastic constants[23].

For a tetragonal crystal of 422 symmetry subject to compressive hydrostatic pressure  $-\sigma$  one can obtain a relation between the pressure derivative of the ordinary refractive index  $n_o$  and the piezooptical coefficients  $\pi_{ij}$  of the form[40]

$$\partial \ln n_o / \partial \sigma = \frac{1}{2} n_o^2 (\pi_{11} + \pi_{12} + \pi_{13}). \quad (\text{B1})$$

Similarly, the pressure derivative of the extraordinary refractive index  $n_e$  is

$$\partial \ln n_e / \partial \sigma = \frac{1}{2} n_e^2 (2\pi_{31} + \pi_{33}). \quad (\text{B2})$$

To obtain the desired  $\partial \ln n_i / \partial P$  from eqns (B1) and (B2) we therefore need only to evaluate the  $\pi_{ij}$  from the measured photoelastic coefficients  $p_{ij}$ . Using the relation

$$\pi_{ij} = p_{ik} s_{kj} \quad (\text{B3})$$

and the compliances  $s_{ij}$  one immediately obtains the  $\pi_{ij}$  and thus  $\partial \ln n_o / \partial P$  and  $\partial \ln n_e / \partial P$ . These quantities are tabulated in Table 10 for wavelengths of 0.488  $\mu$  and 1.15  $\mu$ . It should be noted that while the  $\partial \ln n_i / \partial P$  are required at 0.488  $\mu$  for the Brillouin analysis and in the long wavelength limit for the dielectric analysis, the  $p_{ij}$  have been measured only at 0.63  $\mu$ . The derivatives given in Table 10 were obtained assuming the  $\pi_{ij}$  are frequency independent over this wavelength range and the differences between the values at the two frequencies reflect the dispersion of  $n_o$  and  $n_e$ .

To analyze the uniaxial stress measurements of the  $\epsilon_{\infty,i}$  the dependences of  $n_i$  on uniaxial stress  $\sigma_i$  are required. For the application of a uniaxial stress  $-\sigma_1$  along an  $a$ -axis, one obtains

$$\begin{aligned} \partial \ln n_1 / \partial \sigma_1 &= \frac{1}{2} n_o^2 \pi_{11}, \\ \partial \ln n_2 / \partial \sigma_1 &= \frac{1}{2} n_o^2 \pi_{12}, \\ \partial \ln n_3 / \partial \sigma_1 &= \frac{1}{2} n_e^2 \pi_{31}. \end{aligned} \quad (\text{B4})$$

In eqn (B-4) axis 2 refers to the  $a$  axis perpendicular to  $\sigma_1$  and axis 3 refers to the  $c$ -axis. We note that the crystal becomes biaxial for a  $\sigma_1$  stress; furthermore  $\partial \ln n_1 / \partial \sigma_1$  is negative. Similarly, for a uniaxial stress  $-\sigma_3$  parallel to  $c$ , one obtains

$$\begin{aligned} \partial \ln n_1 / \partial \sigma_3 &= \partial \ln n_2 / \partial \sigma_3 = \frac{1}{2} n_o^2 \pi_{13} \\ \partial \ln n_3 / \partial \sigma_3 &= \frac{1}{2} n_e^2 \pi_{33}. \end{aligned} \quad (\text{B5})$$

For this case, the crystal remains uniaxial and the stress derivative  $n_o$  is given by  $\partial \ln n_1 / \partial P$ . These uniaxial stress derivatives are also included in Table 10.

Finally, we note that to obtain the pressure derivative of  $\epsilon_{\infty}$  for any of the cases discussed above, one need only use the relation

$$\partial \ln \epsilon_{\infty,i} / \partial \sigma_i = 2(\partial \ln n_i / \partial \sigma_i). \quad (\text{B6})$$